



Solving the sulfur isotope discrepancy in Central America

Ally Peccia ^{a,*}, Terry Plank ^a, Shuo Ding ^{a,b}, Louise Bolge ^a, Alessandro Aiuppa ^c, Salvatrice Vizzini ^{c,d}, Cecilia Tramati ^{c,d}, Zoltán Taracsák ^{e,f}, David M. Pyle ^f, Tamsin A. Mather ^f

^a Lamont Doherty Earth Observatory, Columbia University, Palisades, NY 10964-8000, USA

^b Department of Geological Sciences, University of Florida, Gainesville, FL, 32611, USA

^c Dipartimento di Scienze Della Terra e Del Mare, Università di Palermo, 90123 Palermo, Italy

^d Consorzio Nazionale Interuniversitario per le Scienze del Mare, CoNISMa, 00196 Roma, Italy

^e Department of Earth Sciences, University of Cambridge, Cambridge CB2 3EQ, UK

^f Department of Earth Sciences, University of Oxford, Oxford OX1 3AN, UK



ARTICLE INFO

Editor: S Aulbach

Keywords:

Sulfur subduction cycle
Central American volcanic arc
Sulfur isotopes
Volatile cycling
Planetary redox

ABSTRACT

Sulfur has considerable leverage on the redox budget of subducted materials due to its presence as both sulfide (S^{2-}) and sulfate (S^{6+}). Recent work has revealed a discrepancy: arc magmas have positive $\delta^{34}S$ values, while much of the S entering subduction zones should be hosted in pyrite, which is likely to have negative sulfur isotopic values. To address this discrepancy, we focus on the Central American subduction zone, where previous work has revealed positive $\delta^{34}S$ values in parental arc magmas. We report the first comprehensive study of the sedimentary S input to any subduction zone with S concentration and sulfur-isotopic measurements of ODP Site 1040 sediments. Sedimentary S input for Central America is greater than previously thought ($1.71 \pm 0.38 \times 10^8$ mol S/yr/100 km), although insufficient to supply the S output from the arc without contributions from subducting oceanic crust. Furthermore, ~90 % of the sedimentary S input is hosted in pyrite, leading to a bulk sedimentary $\delta^{34}S$ of -19.5‰ . In assessing the mass balance for Central America, we find that selective removal of sulfate does not provide enough S to support arc output and thus, additional S must be mobilized by the oxidation of pyrite with several per mil rock-fluid $\delta^{34}S$ fractionation to positive values. Our results agree with existing evidence that subduction zones act as efficient redox reactors, with oxidized portions of the slab (e.g., altered oceanic crust) providing the oxidizing power to supply sulfate to the arc, while a reduced and ^{32}S -enriched complement sinks into the deeper mantle.

1. Introduction

Subduction zones are key interfaces between surficial and deep Earth reservoirs, facilitating the exchange of materials between the subducting slab, overlying mantle, and volcanic arcs. This interaction is key to the generation and maintenance of Earth's relatively oxygen-rich atmosphere and lithosphere over the last ~ 400 Ma, which exist in contrast to the oxygen-depleted upper mantle (Wood et al., 1990; Kelley and Cotterell, 2009; Lyons et al., 2014; Stolper and Bucholz, 2019). Redox-sensitive elements such as Fe, C, H, and S have multiple valence states, and thus act as the redox levers in any given system, transferring electrons between species and across phases. Clarifying the reservoirs and speciation of each of these elements is paramount to understanding how subduction processes drive the redox evolution of the mantle, surface, and arc volcanism. Although much progress has been made in

recent years, many key questions remain unanswered (Kelley and Cotterell, 2009; Evans, 2012; Brounce et al., 2019; Hirschmann, 2023).

Sulfur in particular remains enigmatic. Arc magmas are elevated in total S concentration, enriched in the heavier ^{34}S isotope, and in sulfate species compared to mid-ocean ridge basalts (Muth and Wallace, 2021). These observations have led to the hypothesis that subduction drives the enrichment of S content in arc magmas through the release of ^{34}S -enriched, sulfate-bearing fluids from the subducted slab (Wallace and Edmonds, 2011; Muth and Wallace, 2022; Beaudry and Sverjensky, 2024). However, recent assessments of S inputs to arcs reveal a discrepancy between arc inputs and outputs: while arc magmas are almost always positive in $\delta^{34}S$ relative to the depleted upper mantle, much of the S entering the subduction zone is hosted in sulfide minerals and thus with negative $\delta^{34}S$ values, e.g., as extreme as -58‰ $\delta^{34}S$ in pyrite (Muth and Wallace, 2021; de Moor et al., 2022; Taracsák et al.,

* Corresponding author.

E-mail address: asp2201@columbia.edu (A. Peccia).

2023; Spruzen et al., 2024). This observation invites three possible solutions: (1) S inputs to arcs are as of yet poorly defined and contain more ^{34}S -rich phases than previously documented, (2) sulfate is preferentially mobilized in slab fluids (Walters et al., 2019; de Moor et al., 2022), thus lending high $\delta^{34}\text{S}$ values in arc magmas, or (3) there is some degree of isotopic fractionation as S is released from the slab during dehydration (Beaudry and Sverjensky, 2024), favoring ^{34}S partitioning into slab fluids/melts. In order to better assess these hypotheses, a careful inventory of subducted S inputs is required. Thus, the primary goal of our study is to provide comprehensive measurements of the S concentration, speciation, and isotopic composition of subducting sediments.

While much progress has been made to better characterize arc outputs in recent years (Muth and Wallace, 2021; de Moor et al., 2022; Taracsák et al., 2023) and to understand redox reactions that happen in subduction zones (e.g., Canil and Fellows, 2017; Walters et al., 2019; Li et al., 2020; Maffeis et al., 2024; Schwarzenbach et al., 2024), estimates of subduction inputs suffer from large uncertainties due to a lack of measurements. Since the pioneering work of Alt and Burdett (1992) on inputs to the Marianas subduction zone, no other study has presented measurements aimed at estimating the flux of S or the bulk sulfur-isotopic composition of subducting sediments or altered oceanic crust at specific convergent margins. Moreover, with their sparse measurements, Alt and Burdett (1992) demonstrated how bulk sedimentary $\delta^{34}\text{S}$ values can vary hugely (by over 40 %) from sample to sample. Recent compilations of the sulfur isotopic composition of sedimentary pyrite similarly document significant heterogeneity in $\delta^{34}\text{S}$ values ($\sim 100 \text{‰}$) as a result of varying depositional conditions (Halevy et al., 2023; Bryant et al., 2023).

Estimating the total flux of sedimentary sulfur and its isotopic composition presents a particular challenge, as the S speciation and $\delta^{34}\text{S}$ values of marine sediments are highly variable and often disseminated in discrete mineral phases, present as sulfate (S^{6+}) and sulfide (S^{2-} , S^-) with their $\delta^{34}\text{S}$ isotopic compositions ranging from as much as +50 % to -60 % (Canfield, 2001a; Canfield et al., 2010; Spruzen et al., 2024). Although sediments make up a smaller proportion of total slab material than the subducting ocean crust, they have the potential to significantly influence sulfur-isotopic signatures at arcs owing to the large potential range in valence state and isotopic composition of sedimentary sulfur. Furthermore, sediments and altered oceanic crust (AOC) likely carry the majority of the redox power in terms of inputs to the subduction zone (e.g., Evans, 2012), as they have been in direct communication with oxygenated surface conditions and may be more readily released than

deeper components of the slab.

Here, we present the first robust inventory of the bulk sedimentary sulfur and associated $\delta^{34}\text{S}$ flux entering any subduction zone, focusing on Central America as a case study. We use an XRF core-scanning approach to assess bulk sulfur and variability in ODP Site 1040 sediments as a reference site for the Central American subduction zone. We develop an ICP-MS technique to calibrate the XRF scans, and then target specific samples for measurements of $\delta^{34}\text{S}$. We observe highly variable, but lithologically systematic $\delta^{34}\text{S}$ values, with the highest sulfur concentrations contained in pyrite-rich clays that have negative $\delta^{34}\text{S}$ values. In assessing the S budget of the Central American arc, we find that preferential recycling of sulfate is insufficient to balance arc outputs, and thus some degree of sulfide oxidation and sulfur isotopic fractionation within the slab is required. Down-going sediments and AOC supply enough sulfur to feed the arc, but must experience fluid-rock isotopic fractionation during sulfide oxidation in order to match the $\delta^{34}\text{S}$ values observed in arc magmas.

1.1. Geologic context

The Central American Volcanic Arc (CAVA; Fig. 1a) serves as the ideal test case for assessing an arc S budget, as its output is one of the best-determined globally based on volcanic gases and melt inclusions, both in terms of S mass fluxes/concentrations and S isotopic composition (Aiuppa et al., 2014; de Moor et al., 2022; Taracsák et al., 2023). Furthermore, slab dip, mantle composition, subducted lithologies, and slab-derived fluid transfer vary significantly along-strike, providing a natural laboratory to examine the influence of tectonic and subduction parameters on S recycling. For example, elevated ^{10}Be , B/La, and Ba/La in Nicaraguan volcanic products suggest significant recycling of the uppermost sediments feeding the arc, with a major contribution from slab-derived fluids (Tera et al., 1986; Carr et al., 1990; Patino et al., 2000; Plank et al., 2002; Bolge et al., 2009). Costa Rica, in contrast, is relatively depleted in the same arc tracers. At the same time, a similar sedimentary section subducts along much of the Central American margin, consisting of units unusually rich in organic carbon and carbonate, providing the opportunity to explore the behavior of sulfur in these lithologies and with these redox drivers.

We focus on ODP Site 1040 (Fig. 1), which penetrated the entire ~300 m (372–651 m below sea floor, mbsf) sedimentary package between the décollement (the boundary between accreted and subducted sediments, identified via seismic imaging) and the basement (Fig. 1b).

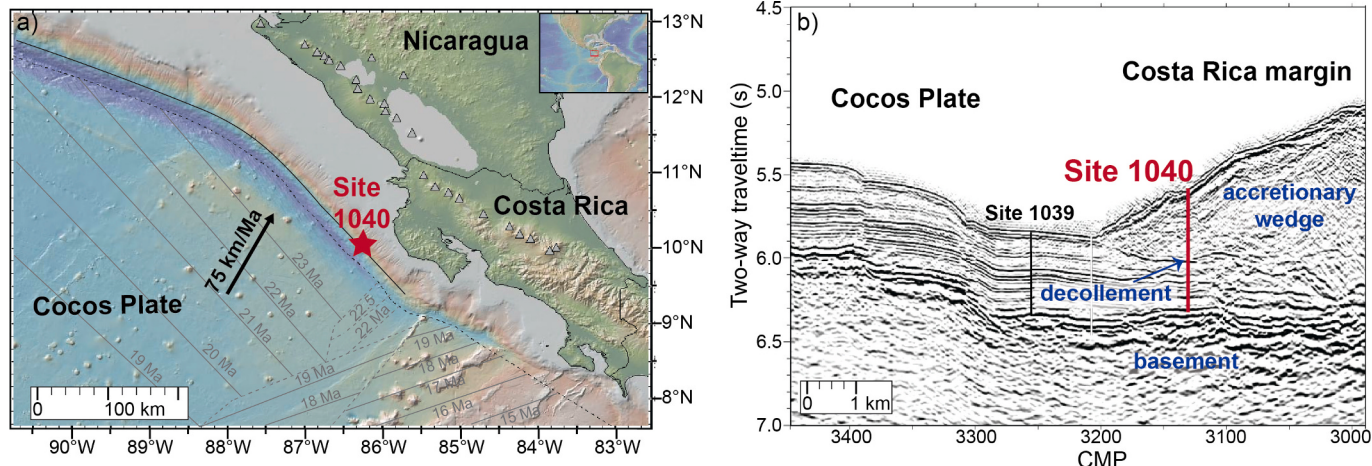


Fig. 1. (a) Map showing the location of Ocean Drilling Program Site 1040 relative to the Nicaragua and Costa Rica portion of the Central American Volcanic Arc and associated volcanoes (triangles), modified from de Moor et al. (2022) and produced with the GeoMapApp (<http://www.geomapapp.org>) CC BY / CC BY (Ryan et al., 2009). (b) Multichannel seismic profile illustrating the position of ODP Site 1040 relative to the subducting plate, modified from Morris et al. (2002). Drilling at Site 1040C penetrated through the accretionary wedge and décollement zone to intersect the underthrust sediments, reaching the gabbro basement at a depth of 653.3 mbsf (Kimura et al., 1997).

The coring intersected three lithological units, from top to bottom: a brown, clayey diatomite with ash layers and abundant pyrite; a silty claystone deposited at low sedimentation rates with high barite concentrations; and a siliceous carbonate deposited before the “carbonate crash” that occurred during the tectonic closure of the Panama Isthmus (Fig. 2; Kimura et al., 1997). The lithologies recovered at Site 1040 are similar to those recovered outboard of the subduction zone at Site 1039, and present a unique opportunity to study the sedimentary sequence being actively subducted. One of the primary objectives of ODP Exp. 170 (during which cores were recovered from Sites 1039 and 1040) was to compare the reference section at Site 1039 with the underthrust sediments at Site 1040. Shipboard and other published work provide excellent context for this study, including major elements, total organic carbon analyses, pore water sulfate, bulk density (Kimura et al., 1997; Kastner et al., 2006) and barite concentrations (Solomon and Kastner, 2012). Previous work has shown differences in the sediment and pore-water geochemistry between these sites, and notably that sulfate reduction continues in the underthrust sediment package, driving enrichment in pyrite and dissolution of barite, both S-bearing minerals (Kimura et al., 1997; Solomon and Kastner, 2012). Therefore, we chose to focus on the cores recovered from Site 1040 to best capture the nature of S in sediments that are eventually subducted to sub-arc depths.

2. Methods

2.1. XRF scanning at the Gulf Coast Repository

XRF scanning of cores from Site 1040 took place at the International Ocean Discovery Program Gulf Coast Repository (GCR) at Texas A&M University using a 3rd-generation Avaatech XRF Core Scanner over the course of a week in summer 2021. Archive section halves were selected from cores across the 300-m depth range and scanned at a target resolution of approximately one XRF “footprint” (1 cm^2) per 4 cm of core. A set of three rock standards (SARM-4, SARM-2, SARM-45) were measured at the beginning and end of each day-long session to track instrument stability. The measured standard values varied $<0.5\%$ in total signal throughput over the course of the week, requiring no instrument maintenance or recalibration (Fig. S1).

Prior to scanning, section halves were warmed to room temperature, carefully scraped with a glass slide to remove surface contamination, and covered with a single layer of Ultralene plastic film to protect the

XRF collection window. Some sections required repeated scraping to remove visible white sulfate precipitates that formed at the tops of sections, likely due to the standard practice of inserting wet sponges at the tops of core tubes. Porewater may have been wicked by the sponges to the section tops, and then precipitated sulfate as the core dried. We confirmed the quantitative removal of such contamination after several scrapings and scans. Scanning proceeded down the centerline of the section at roughly 4 cm intervals, with an initial run at 10 kV and 0.16 mA with a collection time of 6 s to measure lighter elements (Al, Si, Cl, Ar, K, Ca, Ti, Mn, Fe, Cr, P, S, Mg) and a second at 50 kV and 1.5 mA with a 10s collection time and Cu filter to measure heavier elements (Ba, Ca, Ti, Mn, Fe, Ni, Sr, Rb, Zr, Zn, As, Br, Y, Mo, Ag). Sections near the top of the subducting package were often severely cracked/shattered due to proximity to the décollement (an active major fault zone), necessitating manual input of uneven scanning intervals. Initial scanning of the three major lithologic units described by the expedition science party revealed a large amount of heterogeneity in the upper clay-rich unit (Kimura et al., 1997), guiding higher resolution scanning efforts in those cores. Conversely, regions with relatively homogenous element abundances (e.g., the lower carbonate unit) were sampled sparsely (roughly 1 section per 10 m). In total, spectra for 26 elements were collected in 56 sections ($\sim 30\%$ of the recovered section).

Raw spectra were processed and converted to elemental intensities, expressed as “area-counts”. Spectra were inspected routinely throughout scanning to ensure optimal model fit across the varying lithologies. After processing, the initial dataset was filtered to exclude points with Argon-area counts of greater than 300, which indicates improper seal of the collection window with the core surface and air contamination. After filtering, the dataset provided $\sim 14,000$ measurements of semi-quantitative elemental abundances across depths of 372–651 mbsf.

Selection of discrete core samples in the working section halves was guided by the XRF scanning results, with efforts to target regions of highly elevated S, as well as regions with representative (or “background”) S concentration to aid in calibration (Table S1). When possible, sampling occurred with examination of both the archive and working halves to visually match features of interest and avoid obvious surface contamination.

2.2. Digestion of discrete samples

Processing of discrete samples took place at Lamont-Doherty Earth

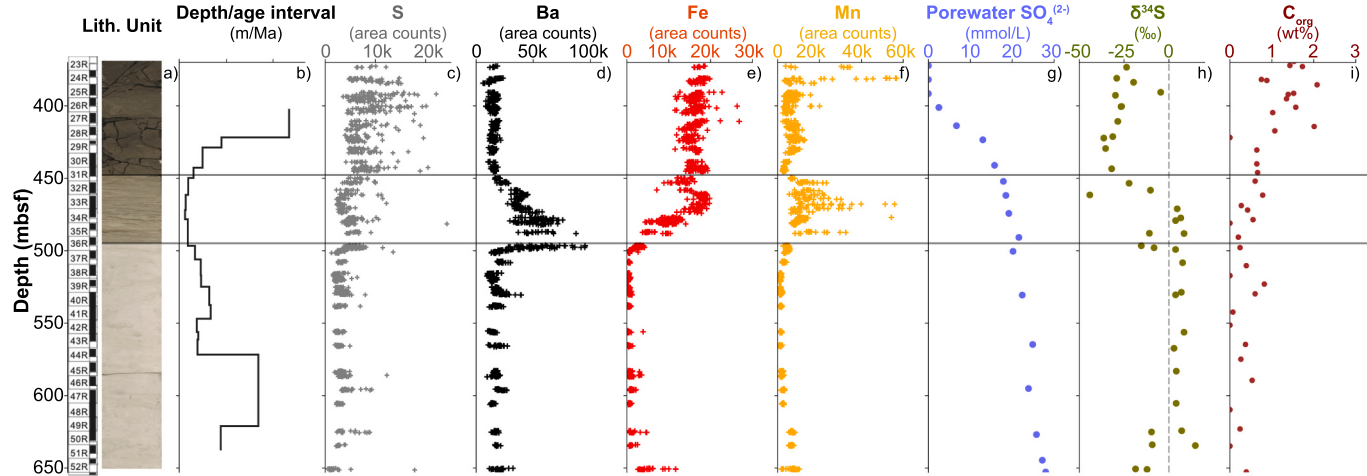


Fig. 2. Downcore recovery and shipboard lithostratigraphic units (a), sedimentation rate (b), porewater sulfate (g) and organic C (i) from Kimura et al. (1997), and XRF elemental abundances of S (c), Ba (d), Fe (e), and Mn (f) from this study. The three notable lithologies (clayey diatomite, silty claystone, and carbonate) are highlighted with representative core photos, taken from individual sections. The abundance of S, Fe, and C_{org} largely follow lithological variations, with the highest concentrations in the uppermost clay lithologies. Ba concentrations are highest where sedimentation rates are low (also marked by high Mn abundance). Similarly, bulk sediment δ³⁴S (h) varies according to lithology, with the most negative bulk δ³⁴S values occurring in the uppermost clay units. Shipboard analysis of porewater sulfate (g) shows active sulfate reduction in the upper ~50 m of the section, consistent with elevated C_{org} concentrations.

Observatory (LDEO) from Fall 2021-Fall 2022, for the purpose of providing high quality ICP-MS sulfur concentration measurements in order to calibrate the XRF core scan data. As some precipitation and mold growth was observed at the GCR, samples were routinely inspected for contamination prior to powdering for sediment digestion. The edges and back of each half round core sample were removed with a clean razor blade to exclude the outer portions of the core (~5 mm) more susceptible to contamination and precipitation of sulfates from pore-water. After freeze-drying, the remaining interior core sample (approximately 2 cm³) was powdered in either a ceramic ball mill or ceramic shatterbox, depending on the size of the sample. Sample digestion was modeled after the procedure described in Erdman et al. (2014). Sediment powders (nominally 50 mg) were weighed “out of the bottle” into 3 ml wrench-top Teflon vials, and then subjected to a hot aqua regia leach. Acids were added by pipetting 1.5 ml of pure concentrated HCl (10 mol/l), followed by 500 µl of pure concentrated HNO₃ (15 mol/l). After combining the acids, vials (with tops closed) were held at 120 °C on a hotplate for 12 h to promote sediment digestion. After cooling, all liquid and remaining residue were carefully transferred to centrifuge tubes with multiple rinses of 3 % HNO₃. Three successive rinses were performed with HNO₃, after centrifuging and pipetting off the supernatant to capture all S in solution. 3 % HNO₃ was then added to a target dilution factor of 2000 (final solution/sample, or ~ 100 ml/50 mg) for ICP-MS analysis. All digestion batches included a blank vial (no sediment), a set of replicates (i.e., two separate aliquots of the same sample), and at least two rock standards (SCO-1, JGb-1, MAG-1) in addition to the unknown samples.

2.3. Measurement of S concentration via ICP-MS

All sample solutions were measured on the Nu Instruments AttoM single collector-high resolution ICP-MS at LDEO at medium mass resolution to resolve ³²S from ¹⁶O¹⁶O interference. S was measured using a single *E*-scan with the magnet mass set at 32.740 amu and peaks centered on ³⁴S, as ³²S and ³³S lie closer to the range of oxygen interference. Samples were aspirated to the spray chamber via a 100 µl/min nebulizer.

Two composite sample solutions were prepared in order to track instrument drift over the course of the ~hour long sessions and to create matrix-matched standards. The composite solutions were prepared by mixing together a few 100 s ml of all the clay-rich sample solutions to create a clay-rich matrix composite, and of all of the carbonate-rich sample solutions to create a carbonate-rich matrix composite. The composite solutions were used to prepare matrix-specific calibration standards that encompassed the range of the unknown solutions, by adding known amounts of a single-component sulfur solution (e.g., using the method of standard additions). Two different standard addition series were made for the carbonate and clay composite solutions.

Collection proceeded with the solution blank measured first, then the carbonate samples, and then the carbonate standards, with carbonate composites measured to monitor drift every four samples. The blank was repeated before beginning the clay sample measurements, which included all rock standards, the clay standard addition series, the clay sample measurements, and the clay composite for drift corrections. The raw intensities of sample and standard measurements were corrected for linear drift between each composite measurement. Solution ppm was calculated using the sulfur standard addition curve by multiplying drift corrected intensities by the standard addition concentration slope. Measured solution ppm is back-calculated to sample ppm by multiplying by the final dilution factor for each sample. These calculations were performed for both ³³S and ³⁴S, which agreed within 2 % for the carbonates and within 4 % for the clays. The average relative standard deviation for duplicate samples was 1 %. Measurement of the blank was below 5 ppm S, and USGS rock standards (JGb-1, MAG-1, SCO-1) measured within 5 % of accepted values (Table S2).

2.4. Sulfur concentration and δ³⁴S values of discrete samples via EA-IRMS

Sulfur concentrations and isotopic compositions in bulk sediment were measured using a ThermoFisher Scientific Isotope Ratio Mass Spectrometer (IRMS Delta V ADVANTAGE) coupled with an Elemental Analyzer (EA Flash 2000) at the University of Palermo during several sessions from Fall 2021 to Summer 2022. Powdered sediment samples (2–25 mg depending on expected concentration) were weighed into tin combustion capsules and mixed with V₂O₅ to ensure complete combustion. Sample concentrations were obtained by total conversion of the sample solid to gas via combustion, with the reaction tube temperature maintained at 1020 °C and a constant helium flow of 140 mL/min. Following combustion and oxidation of the sample to SO₂, the sample passed through the IRMS system where the relative abundance of ³²S to ³⁴S was measured to determine δ³⁴S, expressed in conventional δ unit notation ((³⁴S/³²S)_{sample} / (³⁴S/³²S)_{standard} – 1) as parts per mil (‰) deviations from the international standards, V-CDT (Vienna-Canyon Diablo Troilite). International reference and rock standards (sulfanilamide, SO-6, NBS-127, MAG-1) were analyzed in each batch, with an average standard deviation of ±0.24 ‰ (1σ) from accepted values (Table S2). When possible, duplicate measurements of unknowns were performed, with an average precision of ±0.3 ‰ between replicates. Additionally, standards were mixed in known proportion to test the complete combustion of samples with multiple phases of S present. We find good agreement (<5 % difference) in the expected and measured values for mixtures of the IAEA-S-1 silver sulfide and NBS-127 barite standards (Table S3).

S concentrations determined by EA for rock standards were within 10 % of accepted values. Sulfur concentrations measured via EA generally agree within 10 % of concentrations obtained via ICP-MS, although the ICP-MS technique had higher sensitivity at S concentrations below 200 ppm S.

3. Results

3.1. Downcore element abundance from XRF scans

The resulting XRF dataset provides a high-resolution record of the chemical composition of the down-going sediment package. Downcore major element trends discriminate well the lithological units identified by the shipboard science party, with Al, Ti, and Fe higher in the clay unit overlying a Ca-dominated carbonate unit below (Fig. 2c-f). As noted above, this lithologic change corresponds to the closing of the Panama Isthmus in the Miocene and the subsequent “carbonate crash” (Kimura et al., 1997). The XRF data replicate the observed trend of Ba enrichment in the region 450–500 mbsf (Fig. 2d) noted by both sparse shipboard XRF data of discrete samples (Kimura et al., 1997) and those measured specifically for barite abundance by Solomon and Kastner (2012). Manganese area-counts are also much higher from 450 to 500 mbsf, validating the low sedimentation rates estimated via shipboard biostratigraphy (Fig. 2b, f; Kimura et al., 1997).

Sulfur ranges from a minimum of 500 area-counts near the base of the sedimentary section to a maximum of 75,600 area-counts near the top (Fig. 2c). Repeat scans of core sections yield a relative standard deviation (RSD) of 11 % for sulfur between replicate measurements. Sulfur area-counts are highly variable at the top of the site, likely associated with widespread disseminated pyrite generating surface S enrichments. This agrees well with observations of high organic carbon content and the drawdown of porewater SO₄²⁻ from 375 to 450 mbsf made by Kimura et al. (1997), suggesting ongoing microbial sulfate reduction in these sediments. In contrast, sulfur in the carbonate unit is largely uniform and lower in abundance, reflecting diminished pyrite abundance and overall lower S concentrations (Fig. 2c).

3.2. Calibration with discrete samples

One challenge in calibrating the XRF data is the differing sample footprint of the discrete samples analyzed by ICP-MS and EA. For example, the small spot size and shallow penetration of the XRF source enhances point enrichments of S, while discrete samples include a larger volume and are physically homogenized to better reflect bulk sediment concentration. To address this in our calibration, we employ a dynamic XRF area-count matching technique whereby discrete sample concentrations are related to the rolling average of XRF area-counts with varying window size. A larger window size (20–30 points) was generally chosen for regions of high variability (>30 % RSD within 1 m) and a smaller size (3–10 points) for regions of diminished variability (<30 % RSD within 1 m) or lower data resolution. Point matches were occasionally executed in areas of very low resolution or poor data quality. Additionally, only discrete samples that reflect background and non-anomalous S concentrations were utilized in the calibration. Analysis of a blank sample of pure silica powder (yielding ~250 area-counts, or ~150 ppm S) allows for the assumption that the calibration line passes through the origin.

The resulting calibration shows a linear relationship (R^2 of 0.93) between the bulk S concentration of a sample in ppm and the average XRF S area-counts (Fig. 3a). Given the degree of heterogeneity and multiple phases of S present in the sedimentary sequence, we consider the linear regression to be suitable for direct conversion of XRF area-counts to S concentration.

3.3. $\delta^{34}\text{S}$ values in Central America bulk sediments

The measured $\delta^{34}\text{S}$ values in bulk Central American sediments ($n = 36$) range from -44.1 ‰ to $+14.7\text{ ‰}$, and generally vary according to lithology (Fig. 2h). The upper diatomite and claystone sections (372–460 mbsf) have more negative $\delta^{34}\text{S}$ values (average of -26.6 ‰), while samples from the underlying barite-rich and carbonate units (460–650 mbsf) tend to have positive $\delta^{34}\text{S}$ values ($+0.1\text{ ‰}$ on average). Below 625 mbsf, $\delta^{34}\text{S}$ values become negative once again, though to a lesser degree than in the uppermost sediments. S concentrations tend to be higher in samples with more negative $\delta^{34}\text{S}$ values, suggesting S enrichment due to the presence of pyrite.

3.4. Lowess smoothing and interpolation

In order to produce smoothed downcore profiles for variables of

interest, we employ a combination of Lowess smoothing and linear interpolation from the Statsmodels Python library (Seabold and Perktold, 2010). Lowess smoothing functions, which utilize locally weighted least squares regressions, were applied to downcore calibrated XRF datasets for S and Ba, shipboard measurements of dry bulk density (DBD), and $\delta^{34}\text{S}$ at a given smoothing window width (Fig. 4). A narrower smoothing window (5 % of total depth axis) was applied to the datasets with very high resolution (XRF and DBD), while a wider window (20 %) was applied to the $\delta^{34}\text{S}$ dataset, which has far fewer points. The standard error resulting from Lowess smoothing is calculated from the model residuals. The resulting smoothed profiles were then interpolated linearly at identical depth intervals of 2-cm resolution to allow for operations between datasets. Averages are calculated for the smoothed and evenly sampled dataset for the upper clay vs. lower carbonate units (Fig. 4). Although individual discrete samples and XRF-scanned intervals have highly scattered concentrations, exceeding 1 wt% S in places, the upper clay section has on average 4400 ppm S, a factor of $2.4\times$ higher than the carbonate section (1900 ppm S). The average sulfur content of the entire subducting sedimentary section at Site 1040 is 2900 ppm S. Furthermore, our results agree well with the reported S concentrations measured shipboard by Kimura et al. (1997) (Fig. S2).

4. Discussion

4.1. S speciation and effect on isotopic composition

Assuming sulfur exists only in porewater, barite, and pyrite in Site 1040 sediments, we can calculate the relative proportions of each that contribute to the total sulfur concentration. We make this assumption based on the results of Solomon and Kastner (2012), who show significant barite concentrations in Site 1040 sediments. Similarly, the drawdown of porewater sulfate in the organic C rich clay units suggests the production of diagenetic pyrite (Jørgensen et al., 2019). Thus, barite and pyrite are likely to be the most abundant and stable at depth sulfur-bearing minerals in marine sediments (DHondt et al., 2002; Griffith and Paytan, 2012). Some organic-bound sulfur may be present in the clay unit where C_{org} concentrations are high (375–425 mbsf) and could represent another reservoir of reduced S in addition to pyrite. However, we consider pyrite as the major contributor of sedimentary S, as the high C_{org} sediments occur over a limited depth range, and organic-bound sulfur would have a similar oxidation state and sulfur isotopic composition to pyrite.

Though it is possible that some S is incorporated into the carbonate

Figure 3 consists of two panels, (a) and (b), showing linear calibrations. Panel (a) plots Sulfur concentration (ppm) on the y-axis (0 to 12000) against S area counts on the x-axis (0 to 15000). The data points show a strong positive correlation, with a regression line $y = 0.622x$ and $r^2 = 0.93$. Panel (b) plots Ba concentration (ppm) on the y-axis (0 to 8000) against Ba area counts on the x-axis (0 to 80000). The data points also show a strong positive correlation, with a regression line $y = 0.104x$ and $r^2 = 0.93$. Both panels include a shaded 95% confidence interval and symbols colored by depth, with a color scale from yellow (depth ~400 mbsf) to dark blue (depth ~600 mbsf).

Fig. 3. (a) Linear calibration of XRF S area-counts to sample concentration in ppm S. Error bars represent associated measurement uncertainty between duplicate samples for XRF and ICP-MS techniques. (b) Linear calibration of XRF Ba area-counts to sample concentration as measured by ICP-MS by Solomon and Kastner (2012). Concentrations by ICP-MS are reported dry. Error bars represent associated measurement uncertainty between XRF and 7 % error reported by Solomon and Kastner (2012) for Ba concentration. In both a) and b), symbols are colored by depth.

5

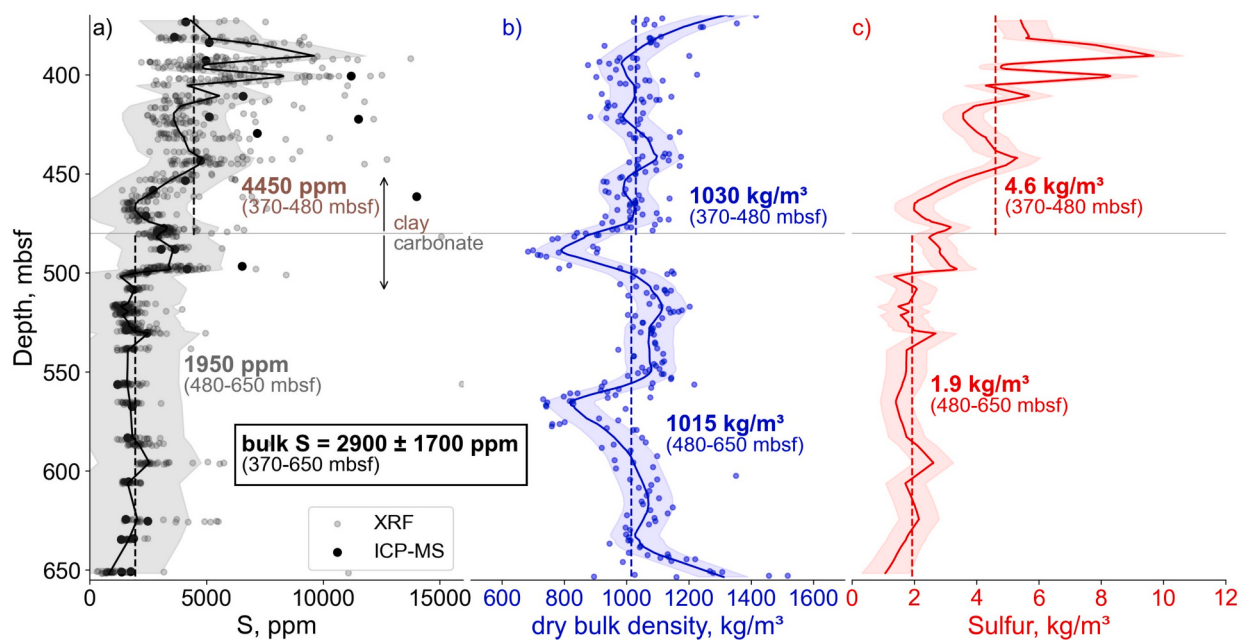


Fig. 4. (a) Downcore S concentration from discrete samples measured by ICP-MS (black filled circles) and the XRF calibrated dataset (gray filled circles), with fitted Lowess regression and 1σ error envelope (b) Shipboard measurements of dry bulk density (DBD), similarly fitted to a Lowess regression with 1σ error envelope. (c) The multiplication of S concentration by DBD produces S concentrations in units of kg/m^3 . Dashed lines denote average concentrations of S for the given depth ranges. The shaded envelope includes DBD Lowess regression error propagated with XRF measurement error and XRF calibration uncertainty. We exclude error from Lowess regression, as variability in the XRF dataset reflects real lithologic surface heterogeneity.

lithologies (“carbonate-associated sulfate”, CAS), CAS is generally only present in the 100 s of ppm S in bulk rocks (Kampschulte and Strauss, 2004). Porewater and barite can be calculated directly, with the remaining sulfur attributed to pyrite. To calculate the amount of S held in porewater, we use the shipboard porewater sulfate concentration (up to $\sim 28 \text{ mM}$, Fig. 4g) and porosity data (Fig. S3) and assume a seawater density of $1030 \text{ kg}/\text{m}^3$. Porewater sulfate makes up only $13 \pm 4 \%$ of the total sedimentary S budget, with very little porewater S from 375 to 425 mbsf due to ongoing sulfate reduction (Table 1; Fig. 2g).

Barium concentration at this site represents barium either held in the mineral barite (BaSO_4) or added from terrigenous sources to the oceans, usually assumed at a roughly constant ratio to aluminum (Dymond et al., 1992; Solomon and Kastner, 2012). Fig. 5a illustrates the low Ba/Al baseline, defined in the 400–500 mbsf clay-rich units, that we take to represent the terrigenous ratio. To calculate the amount of Ba associated with the mineral barite, we assume all Ba in excess of the terrigenous ratio represents the barite-hosted component following Dymond et al. (1992):

$$\text{Ba}_{\text{barite}} = \text{Ba}_{\text{total}} - (\text{Ba}/\text{Al})_{\text{terrigenous}} \times \text{Al}_{\text{bulk}}$$

Table 1
Calculated sedimentary S input, with contributions from pyrite, barite, and porewater S.

	mol S/yr ($\times 10^8$)	\pm (1σ)	% total S	mol S/ yr/100 km ($\times 10^8$)	\pm (1σ)	Bulk $\delta^{34}\text{S}$ (‰) \pm (1σ)
Total S	6.02	1.32	100	1.96	0.428	-14.36
<i>S in pyrite</i>	4.51	1.21	75 %	1.46	0.394	-26.4
<i>S in barite</i>	0.76	0.25	13 %	0.25	0.083	21.5
<i>S in porewater</i>	0.76	0.12	13 %	0.25	0.039	21.5
Total S – porewater corrected	5.27	1.17	87 %	1.71	0.380	-19.5
						3.5

We calculate $\text{Ba}_{\text{barite}}$ directly from Ba and Al XRF area-counts (Fig. 5a) and then convert to Ba concentration using the linear calibration established in Fig. 3b. Following the 1:1 stoichiometric relationship of Ba to S in the mineral barite (BaSO_4), we then relate $\text{Ba}_{\text{barite}}$ concentration directly to S_{barite} (Fig. 5b). In total, barite hosts $13 \pm 3 \%$ of the total sulfur budget in the subducting sedimentary section with the highest concentrations of barite-hosted S found between 460 and 500 mbsf (Table 1; Fig. 6b). Our inferred $\text{Ba}_{\text{barite}}$ concentrations agree well with Barite measured in discrete samples at Site 1039 by Solomon and Kastner (2012), with a modest decrease in $\text{Ba}_{\text{barite}}$ concentration due to ongoing barite dissolution (Fig. S4).

4.2. $\delta^{34}\text{S}$ variations in Central America sediments

We consider the bulk $\delta^{34}\text{S}$ values observed in our sediments to be consistent with known S isotope systematics and the previously described lithologic variations (Fig. 2h). The negative $\delta^{34}\text{S}$ values in the upper diatomite and claystone sections (372–480 mbsf) reflect pyrite-dominated S enrichment, while the barite-rich and carbonate units (480–650 mbsf) have higher $\delta^{34}\text{S}$ values due to the contribution of seawater-derived sulfate (Figs. 2, 6).

While we expect the $\delta^{34}\text{S}$ of seawater sulfate to be limited to +21 to +22 ‰ (the full variation from the modern to Miocene: Paytan et al., 1998), and barite to inherit seawater isotope ratios with little isotope fractionation (Paytan et al., 1998), pyrite may show extreme variation in its sulfur isotopic composition, from +115 to -58 ‰ (Spruzen et al., 2024). Pyrite (FeS_2) forms in diagenetic sedimentary environments, like those of ODP Site 1040, by microbial sulfate reduction (MSR) in sediment porewater and subsequent reaction with iron. Fractionation of S isotopes during MSR leaves the resulting pyrite depleted in ^{34}S . The large variation observed in the $\delta^{34}\text{S}$ of pyrite ($\delta^{34}\text{S}_{\text{pyrite}}$) has classically been explained by both biological and local depositional processes (Canfield, 2001b). Recent work by Halevy et al. (2023) and Bryant et al. (2023) evaluates the role of each of these processes in producing observed variations in the $\delta^{34}\text{S}$ of pyrite ($\delta^{34}\text{S}_{\text{pyrite}}$). Their results suggest that the sulfur isotopic fractionation produced by MSR generally

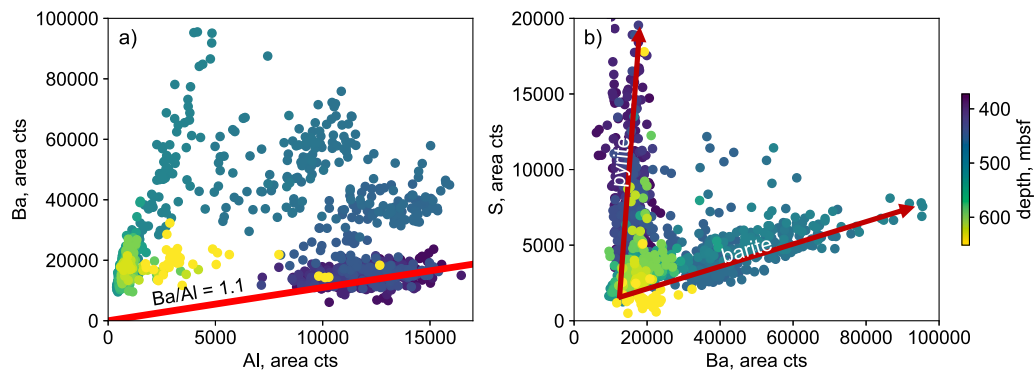


Fig. 5. (a) XRF area-counts of Ba vs. Al, with the red line denoting an assumed terrigenous ratio of Ba/Al of 1.1. All Ba above this line is assumed to be hosted in barite. (b) Plot of XRF area-counts of Ba vs. S, illustrating the presence of significant barite at 475–500 mbsf. “Excess” S above the barite vector represents S hosted in pyrite and porewater sulfur. Dots are colored by depth in both a) and b). (For interpretation of the references to color in this figure legend, the reader is referred to the web version of this article.)

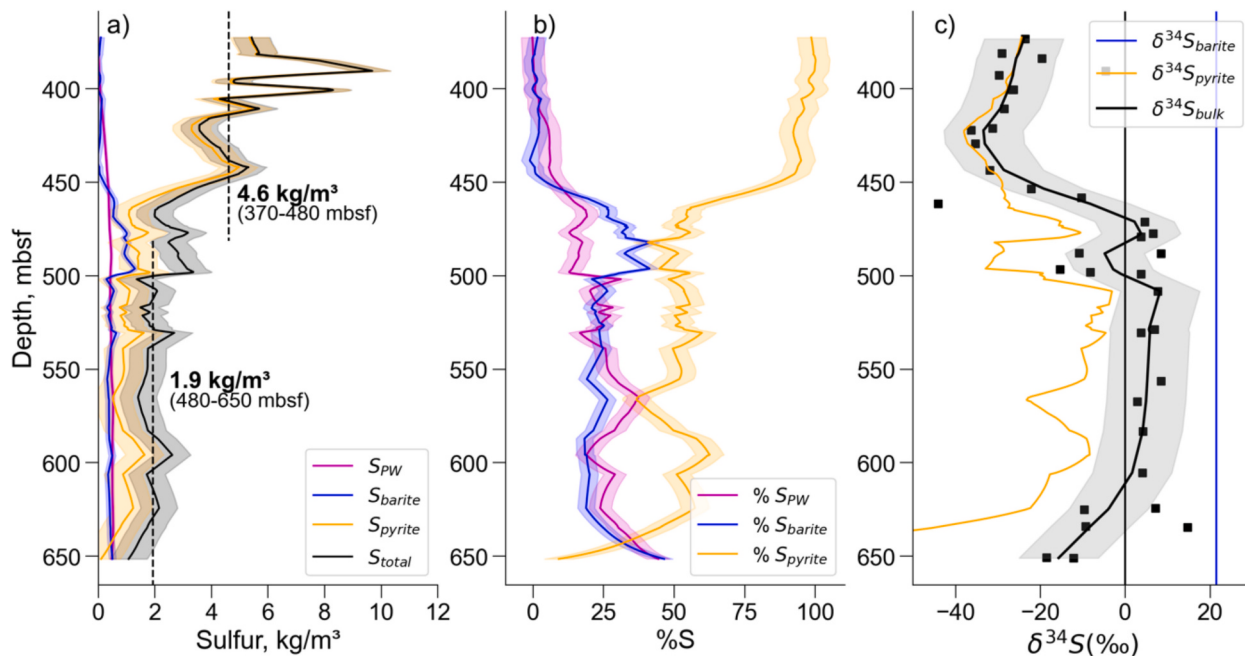


Fig. 6. (a) Downcore plot of the total concentration of S (black) with the contributions from porewater sulfate (magenta), barite (blue), and pyrite (gold) components. Panel (b) shows the relative percent of S held in porewater, barite, and pyrite, calculated from downcore porewater sulfate concentrations (as in Fig. S3) and excess Ba (as in Figs. 5, S4). (c) Downcore $\delta^{34}\text{S}$ in bulk sediment, with measurements of discrete samples (black squares) fit to a Lowess regression (black line). We calculate the $\delta^{34}\text{S}_{\text{pyrite}}$ (gold) from mass balance, assuming porewater sulfate and barite have seawater isotopic compositions ($\delta^{34}\text{S} = +21.5 \text{ ‰}$). $\delta^{34}\text{S}_{\text{pyrite}}$ becomes very negative near the bottom of the core, as the S held in pyrite goes to 0. (For interpretation of the references to color in this figure legend, the reader is referred to the web version of this article.)

operates near S isotope thermodynamic equilibrium between sulfate and sulfide ($\epsilon_{\text{eq}} = -66$ to 78 ‰ , e.g., Wing and Halevy, 2014) in modern sediments, even under conditions with low sulfate concentration. Variations in the $\delta^{34}\text{S}_{\text{pyrite}}$ in modern sediments can thus be best explained by changing depositional conditions that affect the $\delta^{34}\text{S}$ of the porewater sulfate reservoir. This finding is in agreement with the results of Pasquier et al. (2017), who show fluctuations in $\delta^{34}\text{S}_{\text{pyrite}}$ in sediments from the Gulf of Lion are controlled by glacial-interglacial variation in sedimentation rates.

To evaluate the sulfur isotope systematics in the examined sediments, we calculate the $\delta^{34}\text{S}$ of pyrite by assuming $\delta^{34}\text{S}_{\text{barite}}$ and $\delta^{34}\text{S}_{\text{porewater}}$ are $+21.5 \pm 1.0 \text{ ‰}$, as an average of modern seawater ($+21 \text{ ‰}$) and seawater in the Miocene ($+22 \text{ ‰}$), following the $\delta^{34}\text{S}$ record of marine barite (Paytan et al., 1998). Then, we calculate $\delta^{34}\text{S}_{\text{pyrite}}$ from the relative concentrations of porewater-, barite-, and pyrite-associated S

(expressed in wt%) in each interval through the following mass balance relationship:

$$\delta^{34}\text{S}_{\text{pyrite}} = [(\delta^{34}\text{S}_{\text{bulk}} * S_{\text{total}}) - (\delta^{34}\text{S}_{\text{PW}} * S_{\text{PW}}) - (\delta^{34}\text{S}_{\text{barite}} * S_{\text{barite}})] / S_{\text{pyrite}}$$

The average $\delta^{34}\text{S}_{\text{pyrite}}$ weighted by the concentration of S in pyrite (wt%) across the entire section is -26.4 ‰ , and the values vary from nearly -40 ‰ at the top of the section (372–450 mbsf) to -5 ‰ around 510 mbsf (Fig. 6c). The negative $\delta^{34}\text{S}_{\text{pyrite}}$ values and high S concentrations at the top of the section at Site 1040 can be best explained by sulfate reduction in the presence of abundant C_{org} and porewater sulfate, producing a significant isotopic fractionation ($\Delta_{\text{pyr}} \equiv \delta^{34}\text{S}_{\text{sulfate}} - \delta^{34}\text{S}_{\text{pyrite}} \approx 50 \text{ ‰}$). We expect that the total consumption of porewater sulfate in the upper $\sim 50 \text{ m}$ of the section and the lack of diffusive resupply from overlying sediments to drive elevated $\delta^{34}\text{S}_{\text{pyrite}}$ relative to expected equilibrium isotope fractionation ($\epsilon_{\text{eq}} = -66$ to 78 ‰ , as

above) from seawater $\delta^{34}\text{S}$ values, which would lend $\delta^{34}\text{S}_{\text{pyrite}}$ values of $-47\text{--}59\text{‰}$.

Below 450 mbsf, the calculated $\delta^{34}\text{S}_{\text{pyrite}}$ is similarly elevated relative to equilibrium isotope fractionation and the $\delta^{34}\text{S}_{\text{pyrite}}$ in the overlying sediments ($\Delta_{\text{pyr}} \approx 30\text{‰}$, Fig. 6c). This shift coincides with the lithologic change from clays to carbonates, where we expect less suitable conditions for pyrite formation due to diminished Fe and C_{org} concentrations (Fig. 2). We expect that the uptake of porewater sulfate in the overlying clays during MSR enriches the porewater sulfate in ^{34}S through Rayleigh fractionation, shifting the calculated $\delta^{34}\text{S}_{\text{pyrite}}$ to heavier values. Up to $+60\text{‰}$ increase in porewater $\delta^{34}\text{S}$ is observed at other sites where the reduction of porewater S is occurring in C_{org} -rich sediments (e.g., Site 1122; Böttcher et al., 2004; Claypool, 2004). Similarly, the $\delta^{34}\text{S}$ of barite in this region may be higher than the assumed seawater value ($+21.5\text{‰}$) as a consequence of ongoing barite dissolution and diagenetic precipitation (e.g., Griffith and Paytan, 2012) and thereby affect the calculated $\delta^{34}\text{S}_{\text{pyrite}}$. An alternative explanation for the relatively positive $\delta^{34}\text{S}_{\text{pyrite}}$ is that the lithologic conditions in the period of carbonate deposition limit the apparent S isotope fractionation from reaching equilibrium values, potentially due to a difference in the microbial activity or the absence of disproportionation reactions that enhance S isotopic fractionation (Canfield and Teske, 1996; Fike et al., 2006; Jones and Fike, 2013).

Additionally, we note a return to isotopically negative bulk $\delta^{34}\text{S}$ measurements in the lowermost section (625–650 mbsf), despite a sharp increase in Ba and barite-associated S (Fig. 6). This may be attributed to the presence of hydrothermal barite, which can have $\delta^{34}\text{S}$ values ranging from $+3\text{‰}$ to 21‰ due to oxidation of magmatic H_2S and subsequent mixing with seawater (Griffith and Paytan, 2012). A gradual increase in Fe XRF area-counts near the base of the sequence (Fig. 2) also supports hydrothermal mineralization, perhaps from enriched fluid flow through the underlying basement. Barite with low $\delta^{34}\text{S}$ values has previously been associated with the 200–300 °C hydrothermal system at the Juan de Fuca Ridge (Hannington and Scott, 1988). Evidence of ^{32}S -enriched barite in this region is also reflected in the calculated $\delta^{34}\text{S}_{\text{pyrite}}$, which approaches -54‰ . Thus, the assumption that $\delta^{34}\text{S}_{\text{barite}}$ is $+21.5\text{‰}$ for this area may not hold. Nevertheless, our estimate of bulk sediment $\delta^{34}\text{S}$ and the total proportion of S in barite is unaffected by these assumptions, as those estimates depend only on measured bulk $\delta^{34}\text{S}$ and Ba concentrations, respectively.

In addition to barite, porewater sulfate contributes a ^{34}S -enriched signature. While porewater sulfate is consumed in the upper part of the core where active MSR is taking place (372–450 mbsf), it returns to seawater concentration ($\sim 28\text{ mM}$) just above the barite interval (Fig. 2g). Solomon and Kastner (2012) argue that progressive consumption of sulfate in the upper part of the sequence will continue to drive barite dissolution as the plate continues arc-ward. This would in turn generate an evolving supply of subducting sedimentary S with less barite and more pyrite at depth than in-situ measurements near the trench, as for Site 1040. However, we note that organic carbon drops off markedly near 450 mbsf, limiting the viability of continued MSR that could generate significant quantities of additional pyrite-bound S (Fig. 2i; Kimura et al., 1997).

The best estimate of the bulk $\delta^{34}\text{S}$ value for the sediments feeding the trench is given by the average of the smoothed $\delta^{34}\text{S}$ regression weighted by the concentration of S (after weighting by the dry bulk density, as described above and in Fig. 4c). This yields a bulk sedimentary $\delta^{34}\text{S}$ of $-14.4 \pm 0.3\text{‰}$. As illustrated in Fig. 6c, the bulk $\delta^{34}\text{S}$ is driven primarily by low $\delta^{34}\text{S}$ values of pyrite-bound S, as pyrite is the largest contributor to S concentrations in Site 1040 sediments. This is particularly evident in the upper clay unit (372–450 mbsf), where porewater sulfate and barite are virtually absent (Fig. 6b). If we remove porewater sulfate from the total weight of S downcore to reflect expected fluid loss in the forearc, the bulk sedimentary $\delta^{34}\text{S}$ becomes even lower: $-19.5 \pm 3.5\text{‰}$.

4.3. Implications for global redox budgets

Given that pore water and barite each host $\sim 13\%$ of the sulfur in the subducting sedimentary section at ODP Site 1040, we estimate 75 % of the sulfide is pyrite-hosted (Table 1). This predominance of sulfide-hosted sulfur has major implications for the bulk isotopic composition and redox budget of the subducting sediments. Further, our findings are completely different from those in Alt and Burdett (1992), who show that most of the sulfur in Marianas Trench sediment is sulfate-hosted and enriched in ^{34}S , due to low pyrite S content (mostly $<100\text{ ppm}$ S in pyrite). The S concentrations observed in Site 1040 sediments are generally much higher than those examined by Alt and Burdett (1992), who report an average of 850 ppm S in the Marianas sediments (vs. 2900 ppm S for Costa Rica sediments). This underscores the wide heterogeneity expected for different subducting sedimentary sections.

In spite of these heterogeneities, several authors have endeavored to estimate the role of sedimentary S in global redox budgets. For example, the budget presented in Evans (2012) takes a simplified approach in estimating the S content of deep-sea sediments by assuming that $\sim 1\text{ wt\%}$ of Fe is available for pyrite formation, thereby producing a maximum S content of 1.15 wt%. The average S content of all calibrated Site 1040 sediments is $\sim 0.3\text{ wt\%}$, far below the estimate of Evans (2012). However, much of the down-going sedimentary package at Site 1040 consists of carbonate which is low in Fe and thus S. The average S content of pyrite-bearing clays where sulfate reduction is complete (372–410 mbsf) is $\sim 0.6\text{ wt\%}$ S, still $\sim 50\%$ of the S content estimated by Evans (2012). As abundant organic C is available to fuel microbial sulfate reduction, the sediments subducting underneath the Central American margin are likely high in terms of sulfide abundance relative to sediments subducting at other trenches. Yet, the average S content still falls short of the estimate taken by Evans (2012). Thus, Evans (2012) likely overestimates the global sedimentary S[−] flux by at least a factor of 2, although this does not significantly affect the conclusions made in the subsequent redox budget which is dominated by Fe and, to a lesser extent, C.

Stolper et al. (2021) estimate the amount of subducted pyrite by exploiting the S/C_{org} ratio observed in marine sediments under “normal” conditions (e.g., deposited in oxygenated water with typical salinities; Berner and Raiswell, 1983). With an average S/C_{org} of 0.38 ± 0.12 , they estimate marine sediments contain an average of $0.18 \pm 0.06\text{ wt\%}$ S and further assume all S is in pyrite. In contrast to the estimate made by Evans (2012), the estimate by Stolper et al. (2021) appears to be an underestimate, given that the average S content in our pyrite-rich sediments is closer to 0.6 wt%. Further, we find that the S/C_{org} ratio in our sediments has an average S_{bulk}/C_{org} ratio of 0.6 and rarely falls below 0.38 (Fig. S5). Comparing the measured C_{org} to the calculated S in pyrite at Site 1040 produces an average of S_{py}/C_{org} ratio of 0.5, still above the 0.38 ratio utilized by Stolper et al. (2021). Thus, the concentrations ascribed by Stolper et al. (2021) represent a minimum, but may be more appropriate for subducting with a different composition than those subducted at the Central American trench.

4.4. Total flux of sulfur entering the Central American Trench

Our data allow for an updated assessment of the S budget in Central America. We use the following equation to calculate the total flux of sulfur in sediments entering the trench (S_{in}) in kg/yr/m of trench length:

$$S_{\text{in}} = r_{\text{conv}} * h_{\text{sed}} * m_s$$

where r_{conv} is the convergence rate in m/yr, h_{sed} is the thickness of the sediment in m, and m_s is the mass of sulfur in each interval in kg/m³. We calculate the mass of sulfur (kg) in each m³ (m_s) by multiplying the smoothed and interpolated S concentration (wt%) by the DBD (kg/m³) (Fig. 4c) and sum the total mass of S across the $\sim 280\text{ m}$ sediment package. A convergence rate (r_{conv}) of $7.57 \pm 0.06\text{ cm/yr}$ (Syracuse and

Abers, 2006) yields an annual S flux of 62.7 ± 13.8 kg of S/yr/m or 1960 ± 430 mol S/yr/m. We calculate the sedimentary S flux for the section of subducting plate formed at the East Pacific Rise (subducting under Nicaragua and the northern part of Costa Rica), as the sediments at Site 1040 lie on this plate. Further, the thickness of sediments overlying the oceanic crust formed at the Cocos-Nazca Ridge to the south is highly variable due to topographical features generated by seamounts and at the Cocos Ridge. When interpolated by the expected lithologic thickness of the clay and carbonate units along-strike (informed by IODP/ODP/DSDP Sites 495, 844, 845, 1381), the predicted sulfur isotopic composition of sediments does not vary significantly (-20 to $-22\text{\textperthousand}$; Fig. S6). We thus consider Site 1040 to be representative of the sediments feeding the arc.

Another challenge that arises when seeking to compare subduction inputs to outputs is that Site 1040 sediments are offset 2.5 Ma younger than the sedimentary material currently beneath the arc (due to the transport time along the slab). As explored in detail by Plank et al. (2002), the U concentrations in modern arc lavas reflect the subduction and recycling of sediments deposited following the closure of the Panama Isthmus (diatomite clays, 10 Ma). In contrast, the predecessor Miocene Coyol arc contains U concentrations closer to MORB due to diminished U content in the earlier subducted sediments. Because no major palaeoceanographic changes have occurred in this region in the last 2.5 Ma and ^{10}Be concentrations in arc lavas suggest the recycling of the uppermost diatomite clays, we expect that the composition of subducting sediments has stayed relatively constant and consider our estimate an acceptable approximation of the sediments currently feeding the arc (Tera et al., 1986).

While S_{in} represents the S flux for every m of trench length feeding the CAVA subduction zone, we opt to express the flux in terms of S/yr/100 km for ease of comparison with previously published estimates and arc S outputs (e.g., de Moor et al., 2022). We calculate uncertainties via Monte Carlo simulations ($n = 10,000$) for each variable and its associated uncertainty, yielding a sedimentary S flux of $1.96 \pm 0.43 \times 10^8$ mol S/yr/100 km for the entire Costa Rica-Nicaragua sector, with the caveat that sediment thickness may vary where seamounts are being subducted. From the previously calculated S in porewater and barite, we estimate that 25 % of the total S is subducted as sulfate with the remaining 75 % held as sulfides. As discussed above, it is likely that the porewater will be lost at ~ 6 km depth (~ 30 km inboard from the trench) due to compaction and heating as subduction progresses and thus, assuming it can escape, lost in the forearc (Spinelli and Underwood, 2004). We do not include S held in porewater in our final arc S budget to the arc itself, and our final value for the sedimentary S input flux of $1.71 \pm 0.38 \times 10^8$ mol S/yr/100 km (Table 1).

4.5. Estimating total sulfur flux from the arc: the “limiting supply” method

A total sulfur output from the Central American arc of 2.9×10^9 mol S/yr/100 km was estimated by de Moor et al. (2022), based primarily on observations of sulfur gas emissions from fumaroles and volcanic vents over the last two decades. As it is possible that this estimate fails to consider sulfur retained within the arc crust, we consider an independent approach here, where the S flux from the arc can be estimated by multiplying the mass flux of magma from the mantle (m_{magma}) to the arc by the S concentration of primary magmas. In order to calculate the magma flux, we adopt a mass balance approach, in which we consider the flux of slab-derived trace elements ($\text{input}_{\text{slab}}$) as limiting to the output flux at the arc. That is, the arc flux for an efficiently recycled element like Ba cannot exceed the input flux into the subduction zone, and this constraint provides an upper limit to the magma flux. In such cases, the slab serves as the limiting supply for arc outputs, and so we call this the “limiting supply” approach to estimating maximum arc magma fluxes. Assuming 100 % recycling efficiency (all of the slab input is returned to the arc) for any given trace element and an estimate for the

contribution from the mantle (C_{mantle}), we can calculate an upper limit to the mass flux required to produce the concentrations observed in primary melts (C_{parental}) with a given density (ρ_{melt}):

$$m_{\text{magma}} = \frac{\text{input}_{\text{slab}}}{(C_{\text{parental}} - C_{\text{mantle}}) * \rho_{\text{melt}}}$$

We apply this approach to the slab-derived element Ba, as it is thought to be efficiently recycled, exists in high concentrations in Central American whole rocks, and is contributed by the mantle in only small amounts (Plank and Langmuir, 1993; Plank and Langmuir, 1998; Patino et al., 2000; Gale et al., 2013). We considered other elements as well (e.g., Pb, Sr, U, Th, etc.), but found Ba to provide the most limiting supply. We estimate the parental Ba concentration by taking the average whole rock Ba concentration of high MgO samples (6–7 wt% MgO) at six volcanic centers in CAVA and correcting for 30 % crystal fractionation (high precision ICP-MS and ICP-AES whole rock analyses downloaded from the GEOROC database; see Table S4). We estimate the mantle-contribution to arc Ba by assuming the background mantle has a D-MORB Ba/Nb ratio of 4.75 (Gale et al., 2013), and multiplying by the average whole rock Nb (as above). The Ba contributed by the mantle is then subtracted from the parental Ba concentration. We emphasize that the Ba contributed by the mantle is minor relative to the whole rock concentrations (average of 6 % of whole rock Ba concentration), and thus does not have a significant effect on our calculated magma mass fluxes.

Here we provide an example of the limiting supply calculation for Cerro Negro: Whole rock Ba concentrations are 250–450 ppm, with ~ 360 ppm Ba and 1 ppm Nb at MgO content of 6 wt% (Fig. S7). We dilute these concentrations by 30 % to estimate the concentration of the parental melt before crystal fractionation (e.g., Sadofsky et al., 2008; 255 ppm Ba and 0.7 ppm Nb). Then, we calculate the Ba contributed by the mantle using the D-MORB Ba/Nb ratio of $4.75 * 0.7$ ppm Nb = ~ 3 ppm Ba (<2 % of the total Ba), leaving 252 ppm Ba to be supplied from the slab. Assuming an arc melt density of 2750 kg/m^3 , and given the total flux of Ba feeding the arc from sediments and AOC (82 kg Ba/yr/m; see Table S4 for details), we find that the arc magma flux cannot exceed $3.3 \times 10^5 \text{ kg/m/yr}$ ($121 \text{ m}^3/\text{m/yr}$ volume flux) without exceeding the Ba slab input (assuming 100 % recycling efficiency).

This approach produces a range of magmatic volume fluxes for the Central American arc of 70 – $150 \text{ m}^3/\text{m/yr}$, consistent with other published estimates (Table S4; Clift and Vanucci 2004: $\sim 110 \text{ m}^3/\text{m/yr}$, Kutterolf et al., 2008: $\sim 50 \text{ m}^3/\text{m/yr}$ from extrusive products). We multiply the magma fluxes by the maximum S concentrations measured in melt inclusions at each volcano (as an approximation of the undegassed parental S concentrations) to produce an average S flux of 3.12×10^9 mol S/yr/100 km (expressed per 100 km for ease of comparison: Table S5). This independent estimate is remarkably similar to the S flux calculated by de Moor et al. (2022) from volcanic gas emissions (2.9×10^9 mol S/yr/100 km), suggesting that S degassing may be a promising avenue for estimating magma flux at other arcs. Furthermore, this method may be useful for estimating volatile fluxes in settings where gas measurements are sparse. Given that the gas-based flux represents a minimum and the limiting supply approach represents a maximum, we take the average as the best estimate: 3.0×10^9 mol S/yr/100 km (Table 2).

4.6. Agreement of sedimentary S flux with existing work

de Moor et al. (2022) calculated a sedimentary S flux of $1.57 \pm 0.27 \times 10^8$ mol/yr/100 km with a bulk $\delta^{34}\text{S}$ of $-11.4\text{\textperthousand}$. Their estimate was based on sparse shipboard and published measurements of total S and Ba concentrations at analog Site 1039, with an assumed isotopic composition of $-20\text{\textperthousand}$ for the pyrite-bearing units and $+21\text{\textperthousand}$ for the barite-bearing units. Our revised estimate indicates a ~ 10 % larger total S flux of $1.71 \pm 0.38 \times 10^8$ mol/yr/100 km with significantly lower bulk

Table 2
Subducting S inputs and arc S outputs in Central America.

Slab input	mol S/ yr/ 100 km (x 10 ⁸)	± (1σ)	% S in sulfate	mol S in sulfate/yr/100 km (x 10 ⁸)	Bulk $\delta^{34}\text{S}$ (‰)	± (1σ)
Sediments ¹	1.71	0.38	14.4 %	0.25	-19.5	3.5
Altered ocean crust ²	15.07	2.15	15.2 %	2.29	3.0	1.6
Primary crust ³	13.79	2.87	0.0 %	0.0	0.1	0.5
Serpentinite ⁴	1.64	0.47	56.6 %	0.93	6.6	1.9
Erosion ⁵	3.64	0.83	15.2 %	0.55	3.0	1.6
Total	35.85	6.69		4.02	0.98	1.26
Arc Output						
All SCAVA (524 km), from de Moor et al. (2022)				Limiting supply approach (see Table S4)		
mol S/ yr (x 10 ⁸)	mol S/yr/ 100 km (x 10 ⁸)					
Erupted magma	0.66	0.13		avg. magma flux (km ³ /km/ My)	126.2	
Non-erupted	7.10	1.35		avg. S concentration (ppm)	2820	
Gas	144.0	27.5		mol S/yr/100 km (x 10 ⁸)	31.2	
Total Average	151.8	29.0				

¹ Values from this study, as described in text. Porewater S is removed from the sedimentary S flux, and bulk $\delta^{34}\text{S}$ adjusted accordingly.

² From the work of Alt and Shanks (2011), as in de Moor et al. (2022).

³ From the work of Alt (1995), as in de Moor et al. (2022).

⁴ Based on estimates made by Alt et al. (2012), as in de Moor et al. (2022).

⁵ Estimate made by Vannucchi et al. (2001), as in de Moor et al. (2022).

$\delta^{34}\text{S}$ of $-19.5 \pm 3.5\text{‰}$, dominated by S in pyrite phases (average $\delta^{34}\text{S}_{\text{Pyrite}} = -26.4\text{‰}$; Table 1). Still, the similarity of a “best guess” estimate by de Moor et al. (2022) based on sparse measurements and simplified isotopic compositions to our revised estimate provides support for this approach in terms of lithology-based estimates of sedimentary S to arcs globally. Li et al. (2020) provide an estimate of the average global subducting sedimentary S of $8.6 \times 10^8 \text{ mol S/yr/100 km}$, significantly higher than what we calculate here for Central America. However, the estimate made by Li et al. (2020) assumes a sediment density of 2.5 g/cm^3 and an average concentration of 0.6 wt\% S (from Evans, 2012). Both the assumed sediment density and the S concentration are a factor of 2 greater than that observed in the Central American sediments (average of 1.2 g/cm^3 and 0.3 wt\% S , respectively); in fact, a density of 2.5 g/cm^3 lies well outside published estimates of the average bulk density of marine sediments (between 1.7 and 1.95 g/cm^3 , e.g., Sykes, 1996). Thus, we consider the global sedimentary S flux in Li et al. (2020) likely to be an overestimate.

Our findings echo the central challenge in balancing arc S inputs and outputs: the $\delta^{34}\text{S}$ value of sediments entering subduction zones is substantially lower than the $\delta^{34}\text{S}$ values recorded in primary arc melts (Alt et al., 2012; Evans, 2012; Muth and Wallace, 2021; Muth and Wallace, 2022; de Moor et al., 2022; Taracsák et al., 2023). Despite the fact that bulk Central American sediment provides a ready explanation for the high ^{10}Be , U/Th and Ba/La of the Central American arc (Carr et al., 1990; Reagan et al., 1994; Patino et al., 2000), our calculated weighted-average bulk $\delta^{34}\text{S}$ for the sediment of -19.5‰ is not consistent with the positive $\delta^{34}\text{S}$ of Central American arc primary melts ($+0.7\text{‰}$ to $+2.2\text{‰}$,

Taracsák et al., 2023), serving as a challenging test ground for balancing arc inputs and outputs. We next consider how to resolve this discrepancy.

4.7. Preferential release of oxidized S from sediments

One resolution to the $\delta^{34}\text{S}$ isotope discrepancy is the preferential release of oxidized S from sediments (and preferential retention of pyrite in the residual slab). Previous work has suggested mobilization of sulfate-bearing S phases when flushed with NaCl-rich fluids released from the underlying crust, leaving behind sulfide minerals (Newton and Manning, 2005). Further, Brounce et al. (2014) show a correlation between the oxidation state of arc melts and enrichment in Ba, implying direct transfer of sedimentary barite from subducted sediments. Such a process would convey ^{34}S -enriched ($\sim +20\text{‰}$) seawater-derived sulfate from the sediments, and provide ample leverage to shift arc sources to positive values, in addition to being an effective oxidizing agent. The question then becomes: is there enough oxidized sulfate in subducting lithologies to supply the arc S flux and S isotopic composition?

4.8. Balancing the sulfur budget in Central America

de Moor et al. (2022) estimate the slab $\delta^{34}\text{S}$ as $+8.0\text{‰}$, from direct measurement of volcanic gases and an assumed mantle $\delta^{34}\text{S}$ of $\sim 0\text{‰}$. However, Taracsák et al. (2023) point out that S isotopic composition of parental magmas can be overwritten by degassing processes and instead opt to analyze $\delta^{34}\text{S}$ directly in primitive olivine-hosted melt inclusions, which indeed have lower $\delta^{34}\text{S}$ values compared to volcanic gases (average primary melt $\delta^{34}\text{S} + 0.7$ to $+2.2\text{‰}$, compared to an average of $+3.8\text{‰}$ in gases). Taracsák et al. (2023) use a Ti-based melting model to estimate that subducted sources supply $\sim 60\text{ \%}$ of the S to the subarc mantle underlying Cerro Negro and Fuego, with the remaining S supplied by the mantle. If 40 \% of the S is supplied from the mantle source, then $1.8 \times 10^9 \text{ mol S/yr/100 km}$ is required from the down-going slab to balance arc outputs (see Table S6). This is the target supply from the slab, with an average slab $\delta^{34}\text{S}$ value of $+1.9$ to $+3.7\text{‰}$ (Taracsák et al., 2023).

Although Taracsák et al. (2023) estimated a lower contribution from the slab underneath Turrialba (at the southeast end of the CAVA), the degree of melting and metasomatism of the mantle source is poorly known and may be affected by the subduction of seamounts. This in turn affects the average slab $\delta^{34}\text{S}$ value predicted by Taracsák et al. (2023), which is $+2.7$ to $+4.7\text{‰}$, depending on the mantle source. Given these uncertainties, we focus our mass balance on the results obtained for Cerro Negro and Fuego, which better represent the portion of the arc being supplied by Site 1040 sediments. We note, however, that our results are likely still relevant for Turrialba if a primitive mantle source is assumed, requiring $\sim 53\text{ \%}$ of slab S with a $\delta^{34}\text{S}$ of $+2.7\text{‰}$.

As shown in Fig. 7a, it is clear that the sediment alone cannot supply enough sulfur to the arc, and so other subducted sources must contribute, such as the oceanic crust, eroded material from the forearc, and serpentinite in the down-going slab. Each of these lithologies host both sulfate and sulfide phases. Barite makes up just $\sim 15\text{ \%}$ of the total sedimentary sulfur subducted under Central America, contributing less than 1 \% of the total S required to feed arc outputs (Fig. 7b). Alt and Shanks (2011) estimate that sulfate makes up about 15 \% of the total S in altered oceanic crust (consisting of the upper 1750 m of subducting oceanic crust). Like de Moor et al. (2022), we assume a similar $\sim 15\text{ \%}$ sulfate in eroded material from the forearc and none in the primary oceanic crust (de Moor et al., 2022). Conversely, sulfur held in serpentinite is estimated to be as high as $\sim 56\text{ \%}$ sulfate (Alt et al., 2012; de Moor et al., 2022), though there are no direct measurements of S in analogous serpentinite samples; thus, this estimate has a high degree of uncertainty.

If we tally all of the sulfate in each of these subducting sources, this only accounts for 30 \% of the output required at the arc (Fig. 7b), and

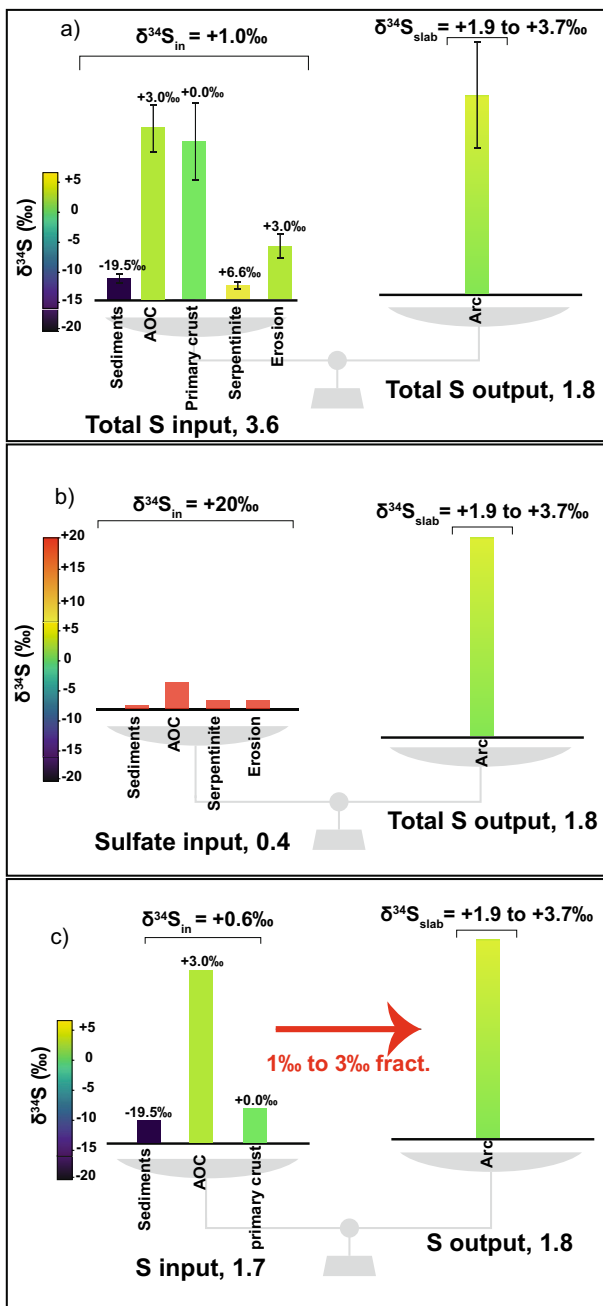


Fig. 7. Schematic illustration of Central America S mass balance between subduction zone inputs and arc outputs (all units are $10^9 \text{ mol S/yr/100 km arc}$ length), with bar lengths proportional to the magnitude of the S flux and colors reflecting bulk $\delta^{34}\text{S}$. The sediment S and $\delta^{34}\text{S}$ estimates come from this study, while other subducted lithologies are from de Moor et al. (2022), with altered ocean crust defined as the upper 1750 m of oceanic crust following the results of Alt and Shanks (2011). The arc S output is the average of de Moor et al.'s estimate and our “limiting supply” approach ($3.0 \times 10^9 \text{ mol S/yr/100 km arc}$; see text for details), with a mantle contribution of ~40 % subtracted. This mantle contribution and the estimated slab contribution to the arc of $\delta^{34}\text{S}$ of $+1.9$ to $+3.7\text{‰}$ are from measurements in Cerro Negro and Fuego melt inclusions by Taracsák et al. (2023). (a) Subduction zones inputs provide more than double the amount of S required to balance the arc, but with a lower bulk $\delta^{34}\text{S}$. (b) Preferential sulfate recycling does not provide enough S to supply the arc. (c) The S flux in sediments, the altered ocean crust (AOC), and a small amount of S the primary crust match the arc output with 80 % removal, producing an isotopic fractionation of ~1–3 % to match the slab $\delta^{34}\text{S}$ contribution to the arc.

yields $\delta^{34}\text{S}$ values that would be too high, presumably close to seawater (~+20 ‰), to match that of the output S. Thus, the arc would require a contribution from subducted sulfide minerals as well, with a bulk $\delta^{34}\text{S}$ of -0.8‰ . Because sedimentary pyrite is more depleted in ^{34}S (−26.4 ‰ on average for Site 1040 sediments) than primary igneous pyrite (around 0 ‰), most of the sulfur in this scenario would need to come from the oceanic crust (e.g., 85 % igneous pyrite and 15 % sedimentary pyrite to equal -0.8‰). Thus, it is possible in this scenario to satisfy the arc composition by removing 100 % of the sulfate from all the subducting lithologies, mixed with some of the pyrite-derived sulfur from oceanic crust and a minor amount of sedimentary pyrite. This scenario is ad hoc, however, and would require the sedimentary pyrite to be mostly retained in the slab, despite the fact that it resides in the highest temperature and most H_2O -rich part of the slab. Additionally, boron isotopic evidence from Central American melt inclusions suggests there is little to no influence from serpentinite dehydration in arc magmas (Turner et al., 2023), in agreement with the thermal model in van Keken et al. (2011) that predicts serpentinite dehydrates beyond the Central American arc. Thus, we do not include S from serpentinite in our following assessment of S flux from the slab. A large degree of uncertainty also surrounds the contribution of material via subduction erosion from the overriding plate. In Central America, such eroded material consists of altered mafic complexes that could be similar in composition to the AOC (de Moor et al., 2022). As such, we do not consider the contribution from subduction erosion in the final mass balance model.

Another possible mechanism is that some sedimentary material is lost in the subduction process before it reaches a depth below the arc, through off-scraping or in diapirs. However, seismic imaging indicates that Central America is a non-accretionary margin and therefore it is unlikely to lose significant sediment in the initial subduction process (Vannucchi et al., 2001). Furthermore, evidence from ^{10}Be in Central American arc lavas requires that sediments from the upper part of the subducting sedimentary package are recycled to the arc (Tera et al., 1986). The high efficiency of Th recycling provides further evidence for the preservation of the subducting sedimentary section under the arc (Plank et al., 2002).

4.9. Subduction zones as redox reactors

Given the result above, whereby the S mass balance and arc sulfur isotopic composition are met by mixing slab sulfate and sulfide in ad hoc proportions, we next consider oxidation and isotopic fractionation of subducted sulfides as an alternative solution to the S-cycling discrepancy through the study of exhumed terranes and application of thermodynamic fluid models (e.g., the Deep Earth Water Model, Perple_X). The results of these studies are either: (1) oxidized sulfur species from the subducted slab (enriched in ^{34}S) are responsible for oxidizing the mantle wedge (Walters et al., 2020; Brounce et al., 2021; Ague et al., 2022) or (2) slab fluids are not oxidizing agents, and crustal differentiation drives oxidation (and increase in $\delta^{34}\text{S}$) in arc magmas (Li et al., 2020; Rezeau et al., 2023). Along the lines of (1), evidence from the exhumed rock record suggests significant redox transfer occurs in subduction zones, although the oxygen fugacity ($f\text{O}_2$) conditions in the slab are debated. Observation of CH_4 -bearing fluid inclusions and textural evidence of sulfide-bearing veins in eclogites and serpentinites suggest reduced fluids prevail at depth (Li et al., 2020; Zhang et al., 2023). However, previous studies noted the prevalence of oxidized species in fluid inclusions in exhumed metamorphic rocks, including sulfate and bisulfate (Frezzotti et al., 2011). Several authors have also explicitly proposed that sulfur isotopic fractionation accompanies the release of oxidized fluids from the slab, explaining high $\delta^{34}\text{S}$ values in arc magmas (Bénard et al., 2018; Walters et al., 2020; Muth and Wallace, 2021; Beaudry and Sverjensky, 2024; Schwarzenbach et al., 2024).

In one such recent study, Beaudry and Sverjensky, 2024 tune the Deep Earth Water (DEW) model for sulfate by incorporating Newton and

Manning's (2005) high pressure anhydrite solubility experimental results, requiring the addition of sulfate complexes of calcium and sodium. They apply the revised model to a range of subduction zone conditions and show that significant concentrations of oxidized sulfur species can be released into slab fluids in equilibrium with pyrite-bearing eclogite at $\text{FMQ} +1.0$ to $+2.0$. Further, the mobilization of pyrite-bound S under these conditions may result in an equilibrium isotopic fractionation between rock and fluid that covers a $\delta^{34}\text{S}$ range from 0 to 10 ‰, the global range of subduction outputs (refer to Fig. 7 in Beaudry and Sverjensky, 2024). The proposed mechanism of pyrite oxidation stems from the thermodynamics fluid modeling by Walters et al. (2020), which suggests that the reduction of Fe^{3+} from the altered ocean crust can produce oxidized, sulfate-bearing fluids.

We consider the combined results from these studies as a satisfactory explanation to the S cycling problem in Central America. For example, if we assume the S held in barite is released into fluid with a $\delta^{34}\text{S}$ value of +21.5 ‰ (i.e., with no sulfur isotopic fractionation) the remaining S required from pyrite is $1.5 \times 10^9 \text{ mol S/yr}/100 \text{ km}$ with a bulk $\delta^{34}\text{S}$ value of −0.8 ‰ (as above). In order to satisfy the slab $\delta^{34}\text{S}$ value range of +1.9 to +3.7 % estimated by Taracsák et al. (2023) for the CAVA, the bulk S released from sulfide oxidation (if released from AOC and sediment indiscriminately) must undergo a sulfur isotope fractionation of only 1–3 %. Following the Beaudry and Sverjensky, 2024 model, the oxidation of pyrite-bound S^- into slab fluid generates a sulfur isotope fractionation that scales depending on the fraction of sulfur removed (Fig. 8). For example, if all the sulfur were removed, there would be no sulfur isotope fractionation. Maximum sulfur isotope fractionation is attained at small fractions removed. On the other hand, if we consider just sediment and AOC as S sources, much of the pyrite-bound S would need to be released to meet arc output, requiring a balance between driving enough sulfur isotope fractionation while providing enough S for the arc. Beaudry and Sverjensky, 2024 predict a fluid-rock sulfur

isotopic fractionation of 1–3 ‰ at 3 GPa and $\text{FMQ} +1$ where 70–80 % of S is lost from the host rock (Fig. 8), putting the bulk slab $\delta^{34}\text{S}$ output in the range of previously published estimates (Taracsák et al., 2023). The sulfur isotope fractionation could be enhanced by a greater degree of S contribution from the primary crust or material introduced from subduction erosion (decreasing the overall % mobilized from host rock to fluid) or at higher slab fO_2 . Thus, we consider preferential sulfate mobilization and a small degree of sulfur isotope fractionation during pyrite oxidation in sediments and the altered ocean crust as the most likely scenario in balancing the Central American S budget (Table S6).

Notably, the models produced by Beaudry and Sverjensky, 2024 consider fluids in equilibrium with mafic and ultramafic assemblages and do not account for differences in subducting sediments, which may further alter the fO_2 of slab fluids and thus the solubility of S (e.g., metasedimentary rocks acting as an “oxidative filter”; Ague et al., 2022). Recent work by Maffei et al. (2024) suggests that the disproportionation of pyrite (S^-) to sulfide (S^{2-}) and sulfate (S^{6+}) species in the AOC and sediments may further increase the oxidizing capacity of fluids transferred from the slab under certain fO_2 conditions. We note, however, that the results of thermodynamic modeling are highly dependent on the prescribed slab fO_2 , which remains a major uncertainty. As noted above, studies of the exhumed rock record have diverging conclusions on whether fluids released are reduced (e.g., Li et al., 2020; Vitale Brovarone et al., 2020; Zhang et al., 2023; Ren et al., 2025) or oxidizing (Frezzotti et al., 2011; Walters et al., 2019; Gerrits et al., 2019; Ague et al., 2022). Although we consider the production of oxidizing fluids to be a suitable assumption for balancing the S budget in Central America, we encourage future studies to reconcile the diverse evidence from field studies across a range of P-T-fO₂ conditions.

5. Conclusions

We began this paper by describing the S isotope discrepancy, in which the isotopic composition of S inputs to subduction zones is lower than the $\delta^{34}\text{S}$ values of arc outputs. In this work, we provide the first robust characterization of subducting sedimentary S sources and bulk $\delta^{34}\text{S}$, using ODP Site 1040 sediments to assess inputs to the Central American arc. The recycling of sediments in the Central American subduction zone has long been recognized, and our study is the first to consider the transfer of sedimentary S. In summary:

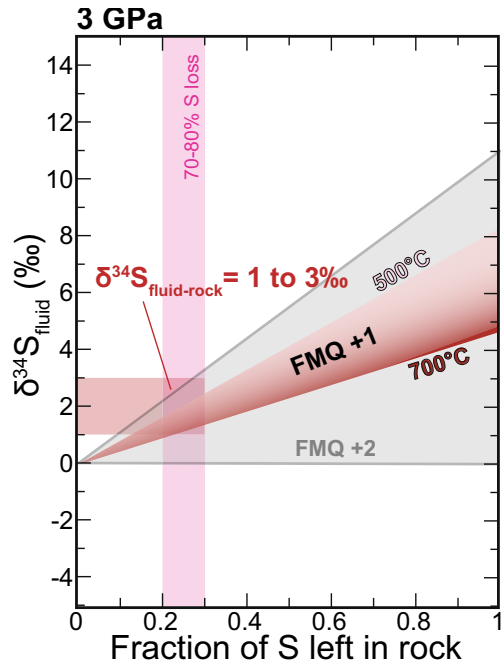


Fig. 8. $\delta^{34}\text{S}$ of slab fluid as a function of amount S released from the slab at 3 GPa assuming an initial slab $\delta^{34}\text{S}$ of 0 ‰. Figure adapted from Fig. 7 of Beaudry and Sverjensky, 2024, predicting the isotopic fractionation associated with the liberation of sulfate and sulfide species from basalt across a range of conditions input to the Deep Earth Water model. We highlight the 1–3 ‰ isotopic fractionation associated with 70–80 % of S removal from the slab at $\text{FMQ} +1$, approximately the fractionation needed to balance arc S flux and $\delta^{34}\text{S}$, as shown in Fig. 8c. The range of isotopic fractionation predicted at $\text{FMQ} +2$ is also shown in gray.

1. We find that S in Central American sediments is hosted primarily in sedimentary pyrite, resulting in a bulk section with low $\delta^{34}\text{S}$ values as it enters the subduction zone. Using our comprehensive data, we estimate a sedimentary S input flux of $1.71 \pm 0.38 \times 10^8 \text{ mol S/yr}/100 \text{ km}$ with a bulk $\delta^{34}\text{S}$ of -19.5 ± 3.5 ‰.
2. In reassessing the total S budget for Central America, we find that although sediments contribute less total S than other sources (e.g., 11 % of that in the altered ocean crust, AOC), their very low $\delta^{34}\text{S}$ of −19.5 ‰ drives the bulk slab $\delta^{34}\text{S}$ towards more negative values.
3. Further, we find in our mass balance that sulfate-derived S sources are insufficient to supply arc outputs and thus, the oxidation of pyrite in sediments and the AOC during subduction is required to mobilize S from the slab.
4. Recent thermodynamic modeling by Beaudry and Sverjensky, 2024 demonstrate how a small degree of sulfur isotope fractionation (increasing $\delta^{34}\text{S} +1$ to 3 ‰) is likely to occur during the oxidation of sulfide at high fO_2 conditions, in turn satisfying the sulfur isotope discrepancy. The residual slab would be consequently enriched in S^{32} , with a bulk $\delta^{34}\text{S}$ of −0.6 to −3.3 ‰.

Our results suggest that the Central American subduction zone acts as an efficient redox reactor, ultimately generating elevated and oxidized S contents in Central American arc magmas in spite of an input of reduced, pyrite-rich subducted sediments. Our preferred mass balance model allows us to reconcile evidence from the exhumed rock record

and resolve the sulfur isotope discrepancy in Central America.

The Central American subduction zone is high in subducting pyrite and has negative sedimentary $\delta^{34}\text{S}$ values relative to other trenches, which are likely sulfate-dominated with lower S contents (e.g., the Marianas: Alt and Burdett, 1992). It is possible the mobilization of sulfur at other arcs does not require or produce a fluid-rock isotopic fractionation, depending on the lithology of the materials subducted, as well as the temperature and oxidation state of the slab. Comparison of the results garnered here at the Central American margin to other trench environments may provide further clarity on the behavior of S in subduction zones and allow for quantitative considerations about Earth's past sulfur cycle and redox history. Critically, the oxidation of sulfide depends on conditions in the slab – the slab fO₂ and thus the degree of required sulfide oxidation is likely to vary from arc to arc, and we emphasize that future studies consider S, Fe and C in tandem when assessing subduction zone redox budgets.

CRediT authorship contribution statement

Ally Peccia: Writing – review & editing, Writing – original draft, Visualization, Validation, Methodology, Investigation, Formal analysis, Data curation, Conceptualization. **Terry Plank:** Writing – review & editing, Validation, Supervision, Resources, Project administration, Methodology, Investigation, Funding acquisition, Conceptualization. **Shuo Ding:** Writing – review & editing, Supervision, Methodology, Investigation, Formal analysis. **Louise Bolge:** Writing – review & editing, Resources, Methodology, Investigation. **Alessandro Aiuppa:** Writing – review & editing, Supervision, Resources, Investigation, Conceptualization. **Salvatrice Vizzini:** Writing – review & editing, Resources, Methodology, Investigation. **Cecilia Tramati:** Writing – review & editing, Resources, Methodology, Investigation. **Zoltán Taracsák:** Writing – review & editing, Conceptualization. **David M. Pyle:** Writing – review & editing, Conceptualization. **Tamsin A. Mather:** Writing – review & editing, Funding acquisition, Conceptualization.

Declaration of competing interest

The authors declare that they have no known competing financial interests or personal relationships that could have appeared to influence the work reported in this paper.

Acknowledgements

This research was supported by NSFGEO-NERC grant “Sulfur cycling in subduction zones” awarded to TP (award no. 1933773) and TAM (NE/T010940/1). We are grateful to Lab Manager Jennifer Hertzberg and Curator Michelle Penkrot at the JRSO XRF Facility located at the Gulf Coast Repository at Texas A&M for assistance in collecting XRF data and sampling legacy core sections. We acknowledge the ODP Expedition 170 Shipboard Science Party, technicians, and crew for their efforts in the collection and cataloguing of sediment cores at Site 1040. We thank Jean Hanley for assistance with preparation of sediment samples at LDEO. Furthermore, we gratefully acknowledge Alberto Malinverno for guidance that contributed to this work. This manuscript was greatly improved by comments from two anonymous reviewers and the editorial handling of Sonja Aulbach. We thank them for their generous efforts.

Appendix A. Supplementary data

Supplementary data to this article can be found online at <https://doi.org/10.1016/j.chemgeo.2025.122901>.

Data availability

The data used in this manuscript is available in the provided electronic data supplement.

References

- Ague, Jay J., et al., Apr. 2022. Slab-derived devolatilization fluids oxidized by subducted metasedimentary rocks. *Nat. Geosci.* 15 (4), 320–326. DOI.org (Crossref). <https://doi.org/10.1038/s41561-022-00904-7>.
- Aiuppa, A., et al., Dec. 2014. Gas measurements from the Costa Rica–Nicaragua volcanic segment suggest possible along-arc variations in volcanic gas chemistry. *Earth Planet. Sci. Lett.* 407, 134–147. ScienceDirect. <https://doi.org/10.1016/j.epsl.2014.09.041>.
- Alt, J.C. “Sulfur Isotopic Profile through the Oceanic Crust: Sulfur Mobility and Seawater-Crustal Sulfur Exchange during Hydrothermal Alteration.” *Geology*, vol. 23, no. 7, July 1995, pp. 585–88. Silverchair, [https://doi.org/10.1130/0091-7613\(1995\)023<0585:SIPTTO>2.3.CO;2](https://doi.org/10.1130/0091-7613(1995)023<0585:SIPTTO>2.3.CO;2).
- Alt, J.C., Burdett, J.W., 1992. Sulfur in Pacific deep-sea sediments (Leg 129) and implications for cycling of sediment in subduction zones. *Proc. ODP Sci. Results* 129, 283–294.
- Alt, Jeffrey C., Shanks, Wayne C., Oct. 2011. Microbial sulfate reduction and the sulfur budget for a complete section of altered oceanic basalts, IODP Hole 1256D (Eastern Pacific). *Earth Planet. Sci. Lett.* 310 (1), 73–83. ScienceDirect. <https://doi.org/10.1016/j.epsl.2011.07.027>.
- Alt, Jeffrey C., et al., Apr. 2012. Recycling of water, carbon, and sulfur during subduction of serpentinites: a stable isotope study of Cerro Del Almirez, Spain. *Earth Planet. Sci. Lett.* 327–328, 50–60. ScienceDirect. <https://doi.org/10.1016/j.epsl.2012.01.029>.
- Beaudry, Patrick, Sverjensky, Dimitri A., 2024. Oxidized sulfur species in slab fluids as a source of enriched sulfur isotope signatures in arcs. *Geochem. Geophys. Geosyst.* 25 (7), e2024GC011542. Wiley Online Library. <https://doi.org/10.1029/2024GC011542>.
- Bénard, Antoine, et al., Aug. 2018. Oxidising agents in sub-arc mantle melts link slab devolatilisation and arc magmas. *Nat. Commun.* 9 (1), 3500. www.nature.com/ezproxy.cul.columbia.edu/. <https://doi.org/10.1038/s41467-018-05804-2>.
- Berner, Robert A., Raiswell, Robert, May 1983. Burial of organic carbon and pyrite sulfur in sediments over Phanerozoic time: a new theory. *Geochim. Cosmochim. Acta* 47 (5), 855–862. ScienceDirect. [https://doi.org/10.1016/0016-7037\(83\)90151-5](https://doi.org/10.1016/0016-7037(83)90151-5).
- Bolge, Louise L., et al., 2009. Correlating geochemistry, tectonics, and volcanic volume along the Central American volcanic front. *Geochem. Geophys. Geosyst.* 10 (12). <https://doi.org/10.1029/2009GC002704>. Wiley Online Library.
- Böttcher, Michael E., et al., Apr. 2004. Microbial sulfate reduction in deep sediments of the Southwest Pacific (ODP Leg 181, Sites 1119–1125): evidence from stable sulfur isotope fractionation and pore water modeling. *Mar. Geol.* 205 (1), 249–260. ScienceDirect. [https://doi.org/10.1016/S0025-3227\(04\)00026-X](https://doi.org/10.1016/S0025-3227(04)00026-X).
- Brounce, M.N., et al., Dec. 2014. Variations in $\text{Fe}^{3+}/\sum\text{Fe}$ of Mariana Arc basalts and mantle wedge fO₂. *J. Petrol.* 55 (12), 2513–2536. Silverchair. <https://doi.org/10.1093/petrology/egu065>.
- Brounce, Maryjo, Cottrell, Elizabeth, et al., Dec. 2019. The redox budget of the Mariana subduction zone. *Earth Planet. Sci. Lett.* 528, 115859. ScienceDirect. <https://doi.org/10.1016/j.epsl.2019.115859>.
- Brounce, Maryjo, Reagan, Mark K., et al., 2021. Covariation of slab tracers, volatiles, and oxidation during subduction initiation. *Geochem. Geophys. Geosyst.* 22 (6), e2021GC009823. Wiley Online Library. <https://doi.org/10.1029/2021GC009823>.
- Bryant, R.N., et al., Nov. 2023. Deconvolving microbial and environmental controls on marine sedimentary pyrite sulfur isotope ratios. *Science* 382 (6673), 912–915 science.org (Atypon). <https://doi.org/10.1126/science.adg6103>.
- Canfield, D.E., 2001a. Biogeochemistry of sulfur isotopes. *Rev. Mineral. Geochem.* 43 (1), 607–636. Silverchair. <https://doi.org/10.2138/gsmg.43.1.607>.
- Canfield, D.E., 2001b. Isotope fractionation by natural populations of sulfate-reducing bacteria. *Geochim. Cosmochim. Acta* 65 (7), 1117–1124. ScienceDirect. [https://doi.org/10.1016/S0016-7037\(00\)00584-6](https://doi.org/10.1016/S0016-7037(00)00584-6).
- Canfield, Donald E., Teske, Andreas, July 1996. Late Proterozoic rise in atmospheric oxygen concentration inferred from phylogenetic and sulphur-isotope studies. *Nature* 382 (6587), 127–132. www.nature.com. <https://doi.org/10.1038/382127a0>.
- Canfield, D.E., et al., “High Isotope Fractionations during Sulfate Reduction in a Low-Sulfate Euxinic Ocean Analog.” *Geology*, vol. 38, no. 5, May 2010, pp. 415–18. Silverchair, <https://doi.org/10.1130/G30723.1>.
- Canil, Dante, Fellows, Steven A., July 2017. Sulphide–sulphate stability and melting in subducted sediment and its role in arc mantle redox and chalcophile cycling in space and time. *Earth Planet. Sci. Lett.* 470, 73–86. ScienceDirect. <https://doi.org/10.1016/j.epsl.2017.04.028>.
- Carr, M.J., et al., Sept. 1990. Incompatible element and isotopic evidence for tectonic control of source mixing and melt extraction along the Central American Arc. *Contrib. Mineral. Petro.* 105 (4), 369–380. Springer Link. <https://doi.org/10.1007/BF00286825>.
- Claypool, George E., 2004. Ventilation of marine sediments indicated by depth profiles of pore water sulfate and $\delta^{34}\text{S}$. In: Hill, Ronald J., et al. (Eds.), *The Geochemical Society Special Publications*, vol. 9. Elsevier, pp. 59–65. ScienceDirect. [https://doi.org/10.1016/S1873-9881\(04\)80007-5](https://doi.org/10.1016/S1873-9881(04)80007-5).
- de Moor, J. Maarten, et al., Jan. 2022. Constraints on the sulfur subduction cycle in Central America from sulfur isotope compositions of volcanic gases. *Chem. Geol.* 588, 120627. ScienceDirect. <https://doi.org/10.1016/j.chemgeo.2021.120627>.
- D'Hondt, Steven, et al., Mar. 2002. Metabolic activity of subsurface life in deep-sea sediments. *Science (New York, N.Y.)* 295 (5562), 2067–2070. PubMed. <https://doi.org/10.1126/science.1064878>.
- Dymond, Jack, et al., 1992. Barium in deep-sea sediment: a geochemical proxy for paleoproductivity. *Paleoceanography* 7 (2), 163–181. Wiley Online Library. <https://doi.org/10.1029/92PA00181>.

- Erdman, Monica E., et al., 2014. Sulfur concentration in geochemical reference materials by solution inductively coupled plasma-mass spectrometry. *Geostand. Geoanal. Res.* 38 (1), 51–60. Wiley Online Library. <https://doi.org/10.1111/j.1751-908X.2013.00226.x>.
- Evans, K.A., June 2012. The redox budget of subduction zones. *Earth-Sci. Rev.* 113 (1), 11–32. ScienceDirect. <https://doi.org/10.1016/j.earscirev.2012.03.003>.
- Fike, D.A., et al., Dec. 2006. Oxidation of the Ediacaran Ocean. *Nature* 444 (7120), 744–747. www.nature.com. <https://doi.org/10.1038/nature05345>.
- Frezzotti, M.L., et al., Oct. 2011. Carbonate dissolution during subduction revealed by diamond-bearing rocks from the Alps. *Nat. Geosci.* 4 (10), 703–706. [www.nature.co m.ezproxy.cul.columbia.edu](http://www.nature.com.ezproxy.cul.columbia.edu). <https://doi.org/10.1038/ngeo1246>.
- Gale, Allison, et al., 2013. The mean composition of ocean ridge basalts. *Geochem. Geophys. Geosyst.* 14 (3), 489–518. Wiley Online Library. <https://doi.org/10.1029/2012GC004334>.
- Gerrits, Anna R., et al., Dec. 2019. Release of oxidizing fluids in subduction zones recorded by iron isotope zonation in Garnet. *Nat. Geosci.* 12 (12), 1029–1033. www.nature.com.ezproxy.cul.columbia.edu. <https://doi.org/10.1038/s41561-019-0471-y>.
- Griffith, Elizabeth M., Paytan, Adina, 2012. Barite in the ocean – occurrence, geochemistry and palaeoceanographic applications. *Sedimentology* 59 (6), 1817–1835. Wiley Online Library. <https://doi.org/10.1111/j.1365-3091.2012.0327.x>.
- Haley, I., et al., Nov. 2023. Sedimentary parameters control the sulfur isotope composition of marine pyrite. *Science* 382 (6673), 946–951 science.org (Atypus). <https://doi.org/10.1126/science.adh1215>.
- Hannington, M.D., Scott, D.S., Sept. 1988. Mineralogy and geochemistry of a hydrothermal silica-sulfide-sulfate spire in the Caldera of Axial Seamount, Juan De Fuca Ridge. *The Canadian Mineralogist* 26 (3), 603–625.
- Hirschmann, Marc M., Oct. 2023. The deep earth oxygen cycle: mass balance considerations on the origin and evolution of mantle and surface oxidative reservoirs. *Earth and Planetary Science Letters* 619, 118311. ScienceDirect. <https://doi.org/10.1016/j.epsl.2023.118311>.
- Jones, David S., Fike, David A., Feb. 2013. Dynamic sulfur and carbon cycling through the end-ordovician extinction revealed by paired sulfate–pyrite δ34S. *Earth Planet. Sci. Lett.* 363, 144–155. ScienceDirect. <https://doi.org/10.1016/j.epsl.2012.12.015>.
- Jorgensen, Bj Barker, et al., 2019. The biogeochemical sulfur cycle of marine sediments. *Front. Microbiol.* 10. <https://doi.org/10.3389/fmicb.2019.00849>. Frontiers.
- Kampschulte, A., Strauss, H., Apr. 2004. The sulfur isotopic evolution of Phanerozoic seawater based on the analysis of structurally substituted sulfate in carbonates. *Chemical Geology* 204 (3), 255–286. ScienceDirect. <https://doi.org/10.1016/j.ch emgeo.2003.11.013>.
- Kastner, Miriam, et al., 2006. Data report: chemical and isotopic compositions of pore fluids and sediments from across the Middle America Trench, Offshore Costa Rica. *Proc. Oc. Drill. Program. Sci. Res.* 205, 1–21.
- Kelley, Katherine A., Cottrell, Elizabeth, July 2009. Water and the oxidation state of subduction zone magmas. *Science* 325 (5940), 605–607. www.science.org.ezproxy.cul.columbia.edu (Atypus). <https://doi.org/10.1126/science.1174156>.
- Kimura, G., et al. (Eds.), 1997. Proceedings of the Ocean Drilling Program, 170 Initial Reports. Ocean Drilling Program. <https://doi.org/10.2973/odp.proc.ir.170.1997>. DOI.org (Crossref).
- Kutterolf, S., et al., 2008. Pacific offshore record of plinian arc volcanism in Central America: 2. Tephra volumes and erupted masses. *Geochemistry, Geophysics, Geosystems* 9 (2). <https://doi.org/10.1029/2007GC001791>. Wiley Online Library.
- Li, Ji-Lei, et al., Jan. 2020. Uncovering and quantifying the subduction zone sulfur cycle from the slab perspective. *Nat. Commun.* 11 (1), 514. DOI.org (Crossref). <https://doi.org/10.1038/s41467-019-14110-4>.
- Lyons, Timothy W., et al., Feb. 2014. The rise of oxygen in earth's early ocean and atmosphere. *Nature* 506 (7488), 307–315. www.nature.com.ezproxy.cul.columbia.edu. <https://doi.org/10.1038/nature13068>.
- Maffeis, Andrea, et al., Mar. 2024. Sulfur disproportionation in deep COHS slab fluids drives mantle wedge oxidation. *Science Advances* 10 (12), eadj2770. www.science.org.ezproxy.cul.columbia.edu (Atypus). <https://doi.org/10.1126/sciadv.adj2770>.
- Morris, J., et al. “¹⁰Be Imaging of Sediment Accretion and Subduction along the Northeast Japan and Costa Rica Convergent Margins.” *Geology*, vol. 30, no. 1, Jan. 2002, pp. 59–62. Silverchair, [https://doi.org/10.1130/0091-7613\(2002\)030<0059:BIOSAA>2.0.CO;2](https://doi.org/10.1130/0091-7613(2002)030<0059:BIOSAA>2.0.CO;2).
- Muth, Michelle J., Wallace, Paul J., June 2021. Slab-derived sulfate generates oxidized basaltic magmas in the Southern Cascade Arc (California, USA). *Geology* 49 (10), 1177–1181. Silverchair. <https://doi.org/10.1130/G48759.1>.
- Muth, Michelle J., Wallace, Paul J., Dec. 2022. Sulfur recycling in subduction zones and the oxygen fugacity of mafic arc magmas. *Earth and Planetary Science Letters* 599, 117836. ScienceDirect. <https://doi.org/10.1016/j.epsl.2022.117836>.
- Newton, Robert C., Manning, Craig E., Apr. 2005. Solubility of anhydrite, CaSO₄, in NaCl–H₂O solutions at high pressures and temperatures: applications to fluid–rock interaction. *Journal of Petrology* 46 (4), 701–716. Silverchair. <https://doi.org/10.1093/petrology/egh094>.
- Pasquier, Virgil, et al., June 2017. Pyrite sulfur isotopes reveal glacial–interglacial environmental changes. *Proceedings of the National Academy of Sciences* 114 (23), 5941–5945 pnas.org (Atypus). <https://doi.org/10.1073/pnas.1618245114>.
- Patino, Lina C., et al., Mar. 2000. Local and regional variations in Central American Arc lavas controlled by variations in subducted sediment input. *Contributions to Mineralogy and Petrology* 138 (3), 265–283. Springer Link. <https://doi.org/10.1007/s004100050562>.
- Paytan, Adina, et al., Nov. 1998. Sulfur isotopic composition of Cenozoic seawater sulfate. *Science* 282 (5393), 1459–1462. www.science.org.ezproxy.cul.columbia.edu (Atypus). <https://doi.org/10.1126/science.282.5393.1459>.
- Plank, Terry, Langmuir, Charles H., Apr. 1993. Tracing trace elements from sediment input to volcanic output at subduction zones. *Nature* 362 (6422), 739–743. www.nature.com.ezproxy.cul.columbia.edu. <https://doi.org/10.1038/362739a0>.
- Plank, Terry, Langmuir, Charles H., Apr. 1998. The chemical composition of subducting sediment and its consequences for the crust and mantle. *Chemical Geology* 145 (3), 325–394. ScienceDirect. [https://doi.org/10.1016/S0009-2541\(97\)00150-2](https://doi.org/10.1016/S0009-2541(97)00150-2).
- Plank, Terry, et al., Dec. 2002. Nicaraguan volcanoes record paleoceanographic changes accompanying closure of the Panama Gateway. *Geology* 30 (12), 1087–1090. Silverchair. [https://doi.org/10.1130/0091-7613\(2002\)030<1087:NVRPCA>2.0.CO;2](https://doi.org/10.1130/0091-7613(2002)030<1087:NVRPCA>2.0.CO;2).
- Reagan, M.K., et al. “Uranium Series and Beryllium Isotope Evidence for an Extended History of Subduction Modification of the Mantle below Nicaragua.” *Geochimica et Cosmochimica Acta*, vol. 58, no. 19, Oct. 1994, pp. 4199–212. ScienceDirect, [https://doi.org/10.1016/0016-7037\(94\)90273-9](https://doi.org/10.1016/0016-7037(94)90273-9).
- Ren, Aijing, et al., June 2025. Subduction-related transfer of sulfur and chalcophile elements recorded in continental mantle wedge peridotites. *Geochimica et Cosmochimica Acta* 398, 11–28. ScienceDirect. <https://doi.org/10.1016/j.gca.2025.04.016>.
- Rezeau, H., et al. “The Role of Immiscible Sulfides for Sulfur Isotope Fractionation in Arc Magmas: Insights from the Talkeetna Island Arc Crustal Section, South-Central Alaska.” *Chemical Geology*, vol. 619, Mar. 2023, p. 121325. ScienceDirect, <https://doi.org/10.1016/j.chemgeo.2023.121325>.
- Ryan, William B.F., et al., Mar. 2009. Global multi-resolution topography synthesis. *Geochem. Geophys. Geosyst.* 10 (3), 2008GC002332. DOI.org (Crossref). <https://doi.org/10.1029/2008GC002332>.
- Sadofsky, Seth J., et al., Apr. 2008. Subduction cycling of volatiles and trace elements through the Central American volcanic arc: evidence from melt inclusions. *Contributions to Mineralogy and Petrology* 155 (4), 433–456 link.springer.com. ezproxy.cul.columbia.edu. <https://doi.org/10.1007/s00410-007-0251-3>.
- Schwarzenbach, Esther M., et al., Aug. 2024. Mobilization of isotopically heavy sulfur during serpentinite subduction. *Science Advances* 10 (32), eadn0641. DOI.org (Crossref). <https://doi.org/10.1126/sciadv.adn0641>.
- Seabold, Skipper, Perktold, Josef, 2010. Statsmodels: econometric and statistical modeling with Python. In: 9th Python in Science Conference.
- Solomon, Evan A., Kastner, Miriam, Apr. 2012. Progressive barite dissolution in the Costa Rica Forearc – implications for global fluxes of Ba to the volcanic arc and mantle. *Geochim. Cosmochim. Acta* 83, 110–124. ScienceDirect. <https://doi.org/10.1016/j.gca.2011.12.021>.
- Spinelli, Glenn A., Underwood, Michael B., 2004. Character of sediments entering the Costa Rica subduction zone: implications for partitioning of water along the plate interface. *Island Arc* 13 (3), 432–451. Wiley Online Library. <https://doi.org/10.1111/j.1440-1738.2004.00436.x>.
- Spruzen, C., et al., Dec. 2024. The sulfur isotopic composition of cenozoic pyrite is affected by methane content and depositional environment. *Earth and Planetary Science Letters* 648, 119097. ScienceDirect. <https://doi.org/10.1016/j.epsl.2024.119097>.
- Stolper, Daniel A., Bucholz, Claire E., Apr. 2019. Neoproterozoic to Early Phanerozoic rise in Island Arc redox state due to deep ocean oxygenation and increased marine sulfate levels. *Proceedings of the National Academy of Sciences* 116 (18), 8746–8755 pnas.org (Atypus). <https://doi.org/10.1073/pnas.1821847116>.
- Stolper, Daniel A., et al., Dec. 2021. The role of the solid earth in regulating atmospheric O₂ levels. *Am. J. Sci.* 321 (10), 1381–1444. www.ajsonline.org. <https://doi.org/10.2475/10.2021.01>.
- Sykes, T.J.S. “A Correction for Sediment Load upon the Ocean Floor: Uniform versus Varying Sediment Density Estimations—Implications for Isostatic Correction.” *Marine Geology*, vol. 133, no. 1, July 1996, pp. 35–49. ScienceDirect, [https://doi.org/10.1016/0025-3227\(96\)00016-3](https://doi.org/10.1016/0025-3227(96)00016-3).
- Syracuse, Ellen M., Abers, Geoffrey A., 2006. Global compilation of variations in slab depth beneath arc volcanoes and implications. *Geochemistry, Geophysics, Geosystems* 7 (5). <https://doi.org/10.1029/2005GC001045>. Wiley Online Library.
- Taracsák, Z., et al., Jan. 2023. Sulfur from the subducted slab dominates the sulfur budget of the mantle wedge under volcanic arcs. *Earth and Planetary Science Letters* 602, 117948. ScienceDirect. <https://doi.org/10.1016/j.epsl.2022.117948>.
- Tera, Fouad, et al., Apr. 1986. Sediment incorporation in island-arc magmas: inferences from ¹⁰Be. *Geochimica et Cosmochimica Acta* 50 (4), 535–550. ScienceDirect. [https://doi.org/10.1016/0016-7037\(86\)90103-1](https://doi.org/10.1016/0016-7037(86)90103-1).
- Turner, Stephen J., et al., Oct. 2023. Boron isotopes in Central American volcanics indicate a key role for the subducting oceanic crust. *Earth Planet. Sci. Lett.* 619, 118289. DOI.org (Crossref). <https://doi.org/10.1016/j.epsl.2023.118289>.
- van Keken, Peter E., et al., 2011. Subduction factory: 4. depth-dependent flux of H₂O from subducting slabs worldwide. *Journal of Geophysical Research: Solid Earth* 116 (B1). <https://doi.org/10.1029/2010JB007922>. Wiley Online Library.
- Vannucchi, Paola, et al., 2001. Tectonic erosion and consequent collapse of the Pacific Margin of Costa Rica: combined implications from ODP Leg 170, seismic offshore data, and regional geology of the Nicoya Peninsula. *Tectonics* 20 (5), 649–668. Wiley Online Library. <https://doi.org/10.1029/2000TC001223>.
- Vitale Brovarone, A., et al. “Subduction Hides High-Pressure Sources of Energy That May Feed the Deep Subsurface Biosphere.” *Nature Communications*, vol. 11, no. 1, Aug. 2020, p. 3880. www.nature.com, <https://doi.org/10.1038/s41467-020-17342-x>.
- Wallace, Paul J., Edmonds, Marie, Jan. 2011. The sulfur budget in magmas: evidence from melt inclusions, submarine glasses, and volcanic gas emissions. *Reviews in Mineralogy and Geochemistry* 73 (1), 215–246. Silverchair. <https://doi.org/10.2138/rmg.2011.73.8>.
- Walters, Jesse B., et al., 2019. Isotopic compositions of sulfides in exhumed high-pressure terranes: implications for sulfur cycling in subduction zones. *Geochimistry*,

- Geophysics, Geosystems 20 (7), 3347–3374. Wiley Online Library. <https://doi.org/10.1029/2019GC008374>.
- Walters, J.B., et al., Apr. 2020. Sulfur loss from subducted altered oceanic crust and implications for mantle oxidation. *Geochemical Perspectives Letters* 36–41. DOI.org (Crossref). <https://doi.org/10.7185/geochemlet.2011>.
- Wing, Boswell A., Halevy, Itay, Dec. 2014. Intracellular metabolite levels shape sulfur isotope fractionation during microbial sulfate respiration. *Proceedings of the National Academy of Sciences* 111 (51), 18116–18125 pnas.org (Atypon). <https://doi.org/10.1073/pnas.1407502111>.
- Wood, Bernard J., et al., Apr. 1990. Mantle oxidation state and its relationship to tectonic environment and fluid speciation. *Science* 248 (4953), 337–345. www.science.org.ezproxy.cul.columbia.edu (Atypon). <https://doi.org/10.1126/science.248.4953.337>.
- Zhang, Lijuan, et al., Jan. 2023. Massive abiotic methane production in eclogite during cold subduction. *National Science Review* 10 (1), nwac207. Silverchair. <https://doi.org/10.1093/nsr/nwac207>.